Experimental investigation of the mechanism for high temperature superconductivity using single of crystals of CLBLCO

Gil Drachuck

Experimental investigation of the mechanism for high temperature superconductivity using single crystals of CLBLCO

PhD Thesis

In Partial Fulfillment of the
Requirements for the
Degree of Doctor of Philosophy

Gil Drachuck

Submitted to the Senate of the Technion - Israel Institute of Technology
Tishrey 5774 HAIFA October 2014

The Research Thesis Was Done Under The Supervision of Prof.Amit Keren
in the Faculty of Physics

Acknowledgements

I would like to thank Prof. Amit Keren for his guidance, support, patience and encouragement during my time in his group.

I would like to thank Assoc. Prof. Amit Kanigel for all his help during my Ph.D.

Special thanks to Galina Bazalizki for helping me with sample preperation and her pleasent company. I thank the lab technicians, Dr. Leonid Iomin and Shmuel Hoida, for their help.

Thanks to all my friends from the low tempreature group for a time well spent.

I would like to thank Assoc. Prof. Amit Kanigel for all his help during my Ph.D.

Special thanks to Lina for her love and patience

Written in memory of Tal Kirzhner.

The Generous Financial Help of the Technion is Gratefully Acknowledged

Publications List

1. **The Fermi surface and band folding in $La_{2-x}Sr_xCuO_4$, probed by angle-resolved photoemission**
E. Razzoli, Y. Sassa, G. Drachuck, M. Mansson, A. Keren, M Shay, Magnus H. Berntsen, O. Tjernberg, M. Radovic, J. Chang, S. Pailhs, N. Momono, M. Oda, M. Ido, O.J. Lipscombe, S.M. Hayden, L. Patthey, J. Mesot, M. Shi
*New Journal of Physics, **12**, 125003 (2010)*

2. **Parallel and perpendicular susceptibility above T c in $La_{2-x}Sr_xCuO_4$ single crystals**
G. Drachuck, M. Shay, G. Bazalitsky, J. Berger, A. Keren
*Physical Review B **85**, 184518 (2012)*

3. **New Perspectives for Cuprate Research:**$Ca_xLa_{1-x}Ba_{1.75-x}La_{0.25+x}Cu_3O_y$ **Single Crystals**
G. Drachuck, M. Shay, G. Bazalitsky, R. Ofer, Z. Salman, A. Amato, C. Niedermayer, D. Wulferding, P. Lemmens and A. Keren
*Journal of Superconductivity and Novel Magnetism **25**, 2331-2335 (2012)*

4. **Anisotropy of the upper critical fields and the paramagnetic Meissner effect in $La_{1.85}Sr_{0.15}CuO_4$ single crystals**
I. Felner and M.I. Tsindlekht, G. Drachuck and A. Keren
*Journal of Physics: Condensesed Matter **25**, 065702 (2013)*

5. **Evolution from a Nodeless Gap to $d_{x^2-y^2}$-Wave in $La_{2-x}Sr_xCuO_4$**
E. Razzoli, G. Drachuck, A. Keren, M. Radovic, N. C. Plumb, J. Chang, Y.-B. Huang, H. Ding, J. Mesot, and M. Shi
*Physical Review Letters **110**, 04700 (2013)*

6. **Comprehensive study of the spin-charge interplay in antiferromagnetic $La_{2-x}Sr_xCuO_4$**
G. Drachuck, E. Razzoli, G. Bazalitski, A. Kanigel, C. Niedermayer, M. Shi and A. Keren
*Nature Communications **5**:3390 (2014)*

7. **Linking dynamic and thermodynamic properties of cuprates: An angle-resolved photoemission study of $(CaLa)_1(BaLa)_2Cu_3O_y$ (x=0.1 and 0.4)**
G. Drachuck, E. Razzoli, R. Ofer, G. Bazalitsky, R. S. Dhaka, A. Kanigel, M. Shi, A. Keren
*Physical Review B **89**, 121119(R) (2014)*

8. **Relation between cuprate superconductivity and magnetism: A Raman study of $(CaLa)_1(BaLa)_2Cu_3O_y$**
D. Wulferding, M. Shay, G. Drachuck, R. Ofer, G. Bazalitsky, Z. Salman, P. Lemmens, A. Keren
*Physical Review B **90**, 104511 (2014)*

9. **Spin and Orbital Excitation Energies Variation with T_c in CLBLCO**
D.S. Ellis, G. Drachuck, R. Ofer, G. Bazalitsky, T. Shmitt, Y. Huang, P. Olalde-Velasco, J Berger, and A. Keren.
Submitted to PRL (2014)

Contents

List of Figures

Abstract

This thesis is present a collection of three experimental research papers in the field of high temperature superconductivity.

We report the successful growth of a large $(\mathrm{Ca}_x\mathrm{La}_{1-x})(\mathrm{Ba}_{1.75-x}\mathrm{La}_{0.25+x})\mathrm{Cu}_3\mathrm{O}_y$ (CLBLCO) single crystal. In this material, x controls the maximum of T_c (T_c^{max}), with minimal structural changes. Therefore, it allows a search for correlations between material properties and T_c^{max}. We demonstrate that the crystals cleave well enough for Raman scattering, ARPES and recently resonant inelastic x-ray scattering (RIXS), and has opened new possibilities for cuprate research.

We also present ARPES data from CLBLCO. We find that the surface doping is independent of the bulk doping or the Ca to Ba ratio. We also demonstrate that the gap can be measured in this system. The hopping parameter t is larger for $x = 0.4$ than for $x = 0.1$ in the overdoped sides. This suggests that T_c^{max} is correlated with electron-orbital overlaps on neighboring sites.

In addition, we investigated the newly discovered nodal gap in hole doped cuprates using a single crystal of antiferromagnetic $\mathrm{La}_{2-x}\mathrm{Sr}_x\mathrm{CuO}_4$. We performed angle resolved photoemission spectroscopy measurements as a function of temperature a nodal gap bellow 45 K. μSR measurements ensured that the sample is indeed antiferromagnetic and that its doping is $x = 1.92\%$, which is below the spin glass phase boundary. We also performed neutron diffraction measurements and determined the thermal evolution of the commensurate and incommensurate magnetic order. Our major finding is that a nodal gap opens at a temperature well below the commensurate ordering at 140 K, and close to the incommensurate spin density wave ordering temperature of 30 K.

Abbreviations

SC	Superconducting/Superconductivity
PG	Pseudogap
FS	Fermi Surface
T_c	SC transition temperature
T_N	Néel temperature
Δ	Gap
High-T_c Superconductivity	HTSC
Bardeen-Cooper-Schrieffer	BCS
$La_{2-x}Ba_xCuO_4$	LBCO
$La_{2-x}Sr_xCuO_4$	LSCO
$YBa_2Cu_3O_{7+x}$	YBCO
$\mathrm{Ca_xLa_{1-x}Ba_{1.75-x}La_{0.25+x}Cu_3O_y}$	CLBLCO
E_f	Fermi level
$\mathbf{k}_f$	Fermi momentum
AFM	Anti-Ferromagnetic/Anti-Ferromagnetism
ARPES	Angle Resolved Photoemission Spectroscopy
NMR	nuclear magnetic resonance
ND	Neutron Diffraction
ρ	Resistivity
EDC	Energy distribution Curve
MDC	momentum distribution Curve
μSR	Muon Spin Rotation
TFZ	Traveling Floating Zone
SDW	Spin Density Wave

Chapter 1

Preface

1.1 High-T_c Superconductivity

The nature of correlated electron system has presented one of the greatest challenges in condensed matter physics, owing to the strong interactions between electrons. The hallmark subject of the past thirty years has been the complete understanding of the mechanism of high-T_c superconductivity (HTSC). While the metallic superconductors were successfully understood withing the framework of Bardeen-Cooper-Schrieffer (BCS) theory [1], there is no one successful description for HTSC to date, despite the enormous number of studies performed to understand its mechanism. HTSC in copper oxides (Cuprates) was discovered in 1986 [2] by Bednorz and Müller. They found superconductivity in the $La_{2-x}Ba_xCuO_4$ (LBCO) compound, were a superconducting transition occurred at $T_c = 30$ K. For comparison, They record until then was about 20 K. Soon after, the $La_{2-x}Sr_xCuO_4$ (LSCO) compound was discovered, pushing superconductivity up to 38 K. The record T_c was broken one year later with the discovery of the $YBa_2Cu_3O_{7+x}$ (YBCO) system having a transition temperature of 91 K [3]. Since then, many high-T_c compounds with even higher transition temperatures have been found. For Mercury based cuprates T_c can reach up to 164 K under high external pressure [4].

The common feature of all high-T_c cuprates is the layered perovskite crystal structure, consisting of CuO_2 planes separated by insulating block layers. Figure 1.1 illustrates a typical CuO_2 plane. The block layers play a role of a charge reservoir. When replacing or adding ions in the block layers, charge is withdrawn from the CuO_2 planes and

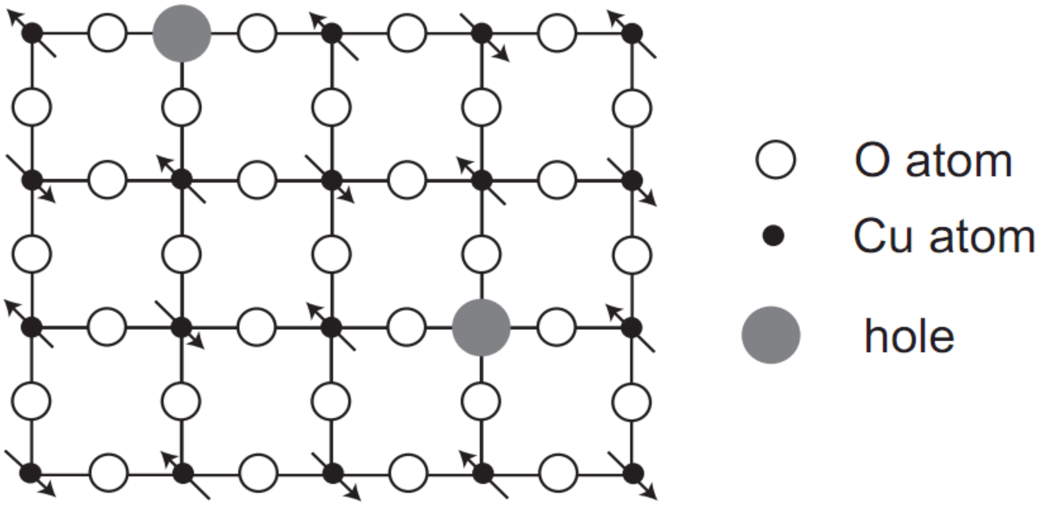

Figure 1.1: Illustration of the Cu-O plane

leaves holes on the copper sites, effectively doping the CuO_2 planes. In practice, hole doping of the planes is achieved in two ways. The first method is by changing the total amount oxygen in the unit cell, which draws charge from the copper sites, as in the YBCO or Bismuth-based cuprates. The second method is by substituting cations in the block layers, with cations which has different oxidation levels. For example, in LSCO the La^{+3} ion is replaced with Sr^{+2}. In contrast to the CuO_2 planes, the block layers are insulating, and have no impact on the low energy electronic states. On the other hand, the CuO_2 planes mainly contribute to the energy states close to the Fermi level (E_f) which dominate the low energy physics of the system, thus setting the stage for superconductivity.

1.2 The Phase Diagram of cuprates

The physical properties of cuprates change drastically with hole (or electron) doping of the CuO_2 planes. A rich phase diagram, with exotic properties has been discovered as the doping x and the temperature T are changed [5]. Figure 1.2 illustrates the phase diagram of hole-doped cuprates as a function of doping. The undpoped parent compounds of cuprates (hole concentration $x = 0$), have a Mott insulator phase, with along range anti-ferromagnetic (AFM) order, and a Néel temperature (T_N) of around 300 K. As the hole concentration increases, the system loses long range magnetic order, while T_N is decreased sharply, until it completely vanishes at $x = 0.02$. For doping beyond $x = 0.02$, for low enough temperatures, the system can either develop a spin-glass phase, which coexists with superconductivity up to $x = 0.08$ [6] (as in LSCO) or immediately enter into a superconducting phase (as in YBCO).

Superconductivity in the cuprates extend between $0.05 < x < 0.27$. The superconducting transition temperature increases with x for "underdoped" samples, achieving a maximum T_c at $x = 0.16$. This is referred to as optimal doping. After this point further doping results in a T_c reduction. This is the "overdoped" side of the phase diagram. The results in the renowned "superconducting dome" in which cuprates exhibit zero resistance and a Meissner effect as in conventional superconductors. However, Phase sensitive experimental techniques, such as angle resolved photoemission spectroscopy (ARPES), clearly showed that at optimally and overdoped samples, the momentum dependence of the gap function has a d-wave symmetry, i.e $2\Delta(k) = \Delta_0(\cos(k_x) - \cos(k_y))$, in contrast to BCS superconductors in which the gap has an s-wave symmetry.

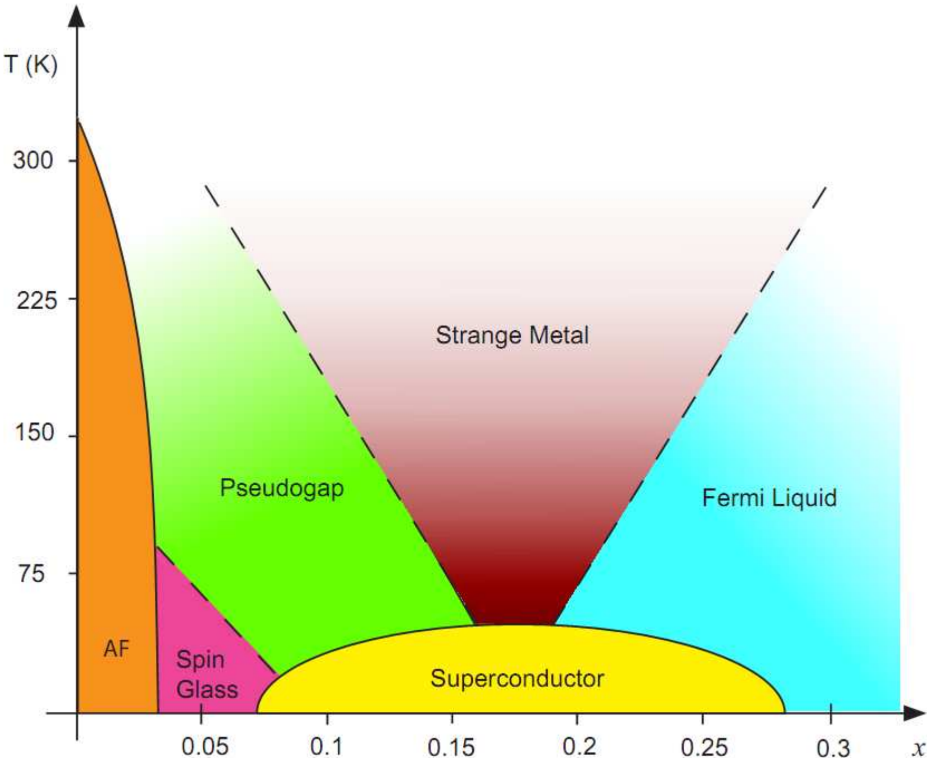

FIGURE 1.2: The generic phase diagram of high-T_c cuprates

While overdoped cuprates behave as a normal metal above Tc, underdoped samples in the normal state show behaviors strongly deviated from the standard Fermi-liquid behavior. An example for the anomalous behavior is observed in the temperature dependence of the resistivity. While Fermi-liquid theory predicts that the temperature dependence of the resistivity, ρ, should be given by $\rho = \rho_0 + AT^2$, an optimally doped $x \sim 0.15$ sample shows a robust T-linear dependence, $\rho = \rho_0 + AT$, in a wide temperature range [7]. This unconventional behavior has been widely observed, for many families of high-T_c cuprates near optimal doping. This region of the phase diagram is referred to as the "Strange Metal"phase. .In the underdoped region, the resistivity exhibits insulating behavior at low temperatures, in the form of logarithmic temperature dependence.

In overdoped cuprates, the SC energy gap vanishes above T_c along the entire Fermi surface, from $(\pi, 0)$-$(0, \pi)$. In the underdoped cuprates however, the energy gap does not vanish above T_c, and is persistent up to a higher temperature (T^*). This energy gap is referred the Pseudogap (PG). Signatures of PG has been observed with experimental techniques such as nuclear magnetic resonance (NMR), optical conductivity, Tunneling and resistivity ([8]). The ungaped part of the Fermi surface (FS) is called the Fermi arc. ARPES measurements revealed the "Fermi arc" is centered around the (π, π), and that the its length scales to T/T^* [9].

The underlying mechanism of the pseudogap remains a subject of great debate in the field of high-T_c cuprates. On one hand, the pseudogap can be interpreted as a precursor of superconductivity in which Cooper pairs are formed without long range order of the superconducting order parameter. On the other hand, the pseudogap can be interpreted as a result of other competing orders unrelated to superconductivity, in the form of a spin or charge density wave, which competes with superconductivity[10, 11]. Moreover, an additional gap in the (π, π) direction (nodal gap) has been observed in underdoped cuprates, such as LSCO, Bi2212 and Bi2201, extending deep into the antiferromagnetic phase [12–14]. .The origin of the nodal gap is extensively discussed the thesis as a published paper.

1.3 The $\mathrm{Ca_xLa_{1-x}Ba_{1.75-x}La_{0.25+x}Cu_3O_y}$ (CLBLCO) System

The $\mathrm{Ca_xLa_{1-x}Ba_{1.75-x}La_{0.25+x}Cu_3O_y}$ (CLBLCO) system is a cuprate superconductor, synthesized at the Technion [15], which provides a unique "experimental playground" and might shed light on the mechanism of superconductivity in the cuprates. CLBLCO crystal structure is similarly to $\mathrm{YBa_2Cu_3O_{6+\mathit{x}}}$. Nevertheless, unlike YBCO, CLBLCO is tetragonal for all values of x and y and has no chain ordering. In addition CLBLCO has two tunable parameters; x, the amount Ca-to-Ba ratio and y, the total of oxygen doping. The crystal structure of CLBLCO is shown in 1.3. In CLBLCO there are two CuO_2 planes, in the center of the unit cell, separated by a Calcium or Lanthanum cation [16, 17]. As the physical properties of CLBLCO strongly depends on both variables, clear systematic changes appear by varying x. Four families of CLBLCO can be defined, with x values of $x = 0.1, 0.2, 0.3$ and 0.4. Although, Each CLBLCO family has a different phase diagram, they share a common origin as will be discussed in the next paragraph.

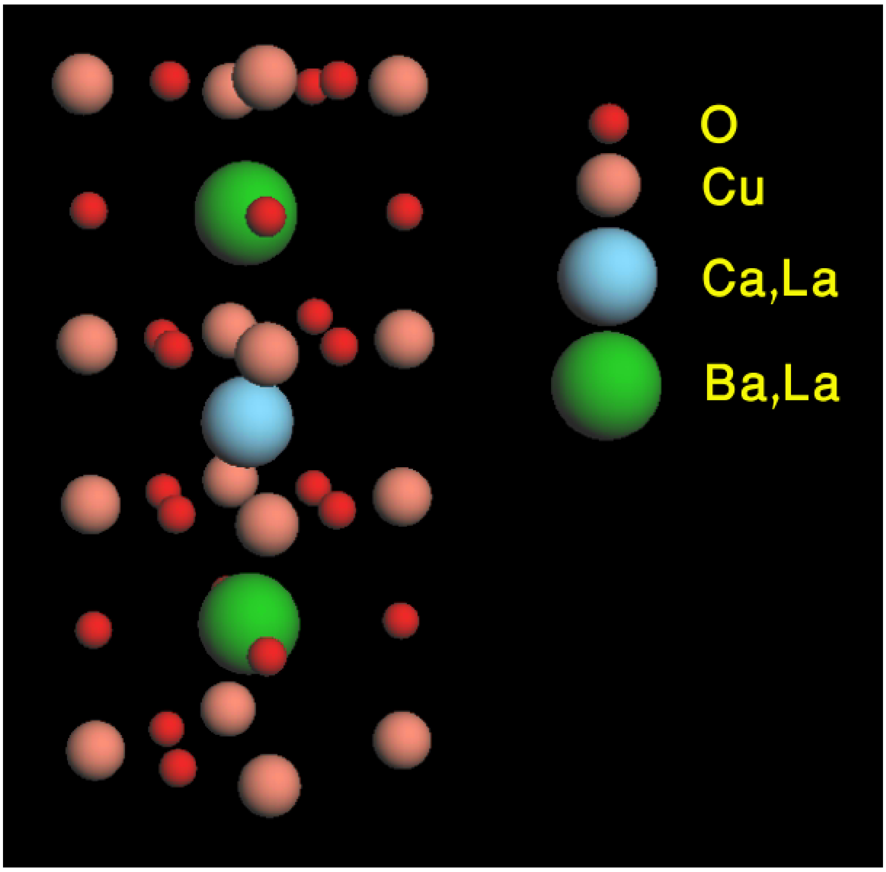

Figure 1.3: The unit cell of CLBLCO

The phase diagram of CLBLCO for various values of x and y is presented in Fig. 1.4(a) [18]. When varying x, the amount of Lanthanum in the chemical formula remains constant, and therefore x stands for the Calcium-to-Barium ratio. The parameter y controls the oxygen level and moves the system between the different phases. At around $y = 7.15$ each family has its maximum T_c [T_c^{max}]. Changing x from 0.1 to 0.4 varies T_c^{max} from 58 K to 80 K [17]; roughly a 30% increase. The variation T_c^{max} between families of CLBLCO is achieved with minute structural changes.

The level of disorder in the CLBLCO system has been investigated by several experimental techniques. The most direct measurement was done by High resolution powder x-ray diffraction (HRPXRD) studies [19]. It was found that Line widths of the (006) and (200) Bragg peaks and the isotropic atomic displacement factor for the Ba/La site, for the optimally doped CLBLCO, slightly increases as x increases. This indicates that disorder is increased, mainly on the Ba site, as more Ca introduced into the system. This, anticipated results, of course cannot explain the increase in Tc as x increases.

A clearer result was obtained by Raman spectroscopy which show that the most pronounced phonon peak at 300cm^{-1} is in fact narrower for the $x = 0.1$ than for the $x = 0.4$ families. The width of this phonon is a measure of the phonon coherence length. The cleaner the material the longer is this length and the narrow is the peak [20]. The Raman scattering measurement indicates that despite its lower Tc, the $x = 0.1$ is cleaner. Finally, NMR on Cu [21], O [18], and Ca [22], show that the line width of all nuclei are the same for both families. The NMR line width is a measure of the local distortions and magnetic impurities next to the detected nuclei. Identical line widths means a similar local environment for both families.

Therefore, *a priori*, T_c^{max} should not depend on x. However, increasing x increases the amount of the Ca^{2+} in the Y site of YBCO at the expense of La^{3+}. This charge transfer is equivalent to reducing positive charge on the (YBCO) Y site and increasing it on the (YBCO) Ba site, and could alter the Cu-O-Cu buckling angle. High resolution neutron diffraction has shown that as x is increased, the Cu-O-Cu bond becomes straighter and shorter [23], while other structural properties remain intact [21]. The bond length and buckling are the major factors that control orbital overlap and, in turn, Fermi velocity and the super-exchange J.

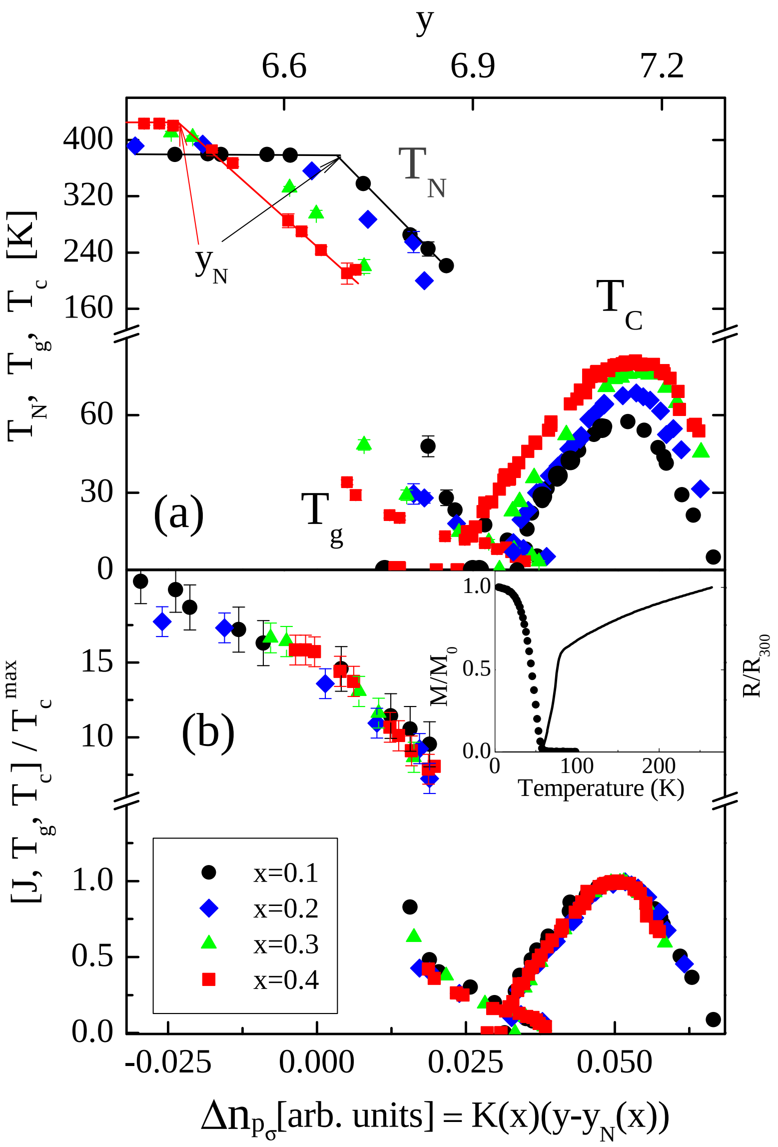

FIGURE 1.4: (a) The phase diagram of CLBLCO showing the Néel (T_N),glass (T_g) and superconducting (T_c) temperatures over the full doping range for the four families. y_N indicates the oxygen level where T_N start to drop. (b) The unified phase diagram of CLBLCO. The critical temperatures, and J extracted from T_N, are divided by T_c^{max} and plotted as a function of doping variation in the oxygen orbital Δn_{p_σ}. Inset: Normalized resistivity and susceptibility as a function of T obtained from an optimally doped crystal with $x = 0.1$.

For example, early muon spin rotation (μSR) measurements using compressed CLBLCO powder samples in the anti-ferromagnetic phase, combined with theoretical calculations, revealed that J is x-dependent, as expected, and that $T_c^{\max}(x) \propto J(x)$ [24]. Similarly, NMR established that simple valence counting does not represent the true doping of the CuO$_2$ planes and that a doping efficiency parameter $K(x)$ should be introduced; the number of holes in the oxygen 2p$_\sigma$ orbital is given by $\Delta n_{2p} = K(x)(y - y_N)$ where

y_N is defined in Fig. 1.2(a) [18]. The most striking feature of the CLBLCO system is revealed, when plotting $J(x)$, T_g, and T_c normalized by $T_c^{\max}(x)$ as a function of Δn_{2p}. All critical temperature and critical doping are scaled and unified phase diagram is appears, as depicted in Fig. 1.4(b) [18, 24].

1.4 The $La_{2-x}Sr_xCuO_4$ (LSCO) system

The crystal structure of the $La_{2-x}Sr_xCuO_4$ (LSCO) system is shown in Fig.1.5. The insulating block layer of LSCO is a double La-O, which play the role of a charge reservoir. The La-O layers are ionic and do not contribute to the low-energy electronic states (~ 1 eV). When replacing La^{+3} with Sr^{+2}, charge is withdrawn from the CuO_2 effectively serving as a dopant. Out of all high T_c cuprates, LSCO has the simplest crystal structure which making it advantageous for studying the CuO_2 planes. In addition, The block layer has neither the Cu-O chains which affect the CuO_2 plane of YBCO, nor the complicated structural modulation present in the block layer of Bi2212.

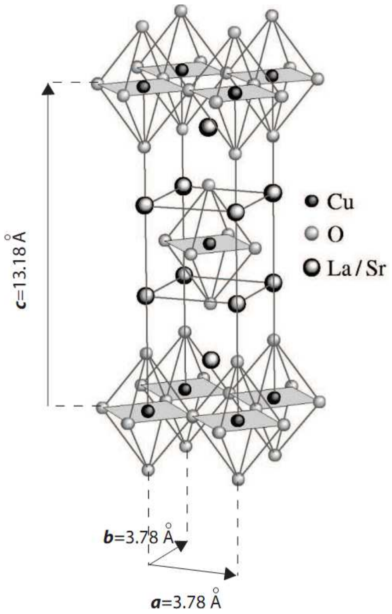

FIGURE 1.5: The crystalline structure of $La_{1-x}Sr_xCuO_4$. (adapted from [25])

The phase diagram of LSCO is the generic one of all cuprates (described in 1.2) ranging from the antiferromagnetic Mott insulator, through a spin-glass phase, down to superconductivity. However, on the superconducting dome, a slight suppression of T_c is present, around the $x = 1/8$ hole concentration (so-called 1/8 anomaly). This suppression of T_c is more pronounced in related materials such as $La_{2-x}Ba_xCuO_4$ and

$La_{1.6-x}Nd_{0.4}Sr_xCuO_4$ at equal hole doping. Inelastic neutron scattering (INS) revealed dynamical incommensurate spin and charge fluctuations in LSCO at the "magic doping and throughout the underdoped region. It was proposed by Tranquada *et al.* [26] that the static spin and charge order in LSCO has a form of stripes while the suppression of T_c is a result of stripe order which is stabilized by at a hole concentration of $x = 1/8$.

1.5 Motivation

While the work presented in the previous section deliver important understanding of the CLBLCO system, μSR is not known to be a direct probe of J and more profound work was needed to clarify the relation between the superconducting and magnetic energy scales. Inelastic neutron and Raman scattering are more appropriate for a direct determination of J. Moreover one can relate the super-exchange to the nearest neighbor hopping term t which can be extracted from ARPES measurements. These advanced measurements require large single crystals with specific orientation and high quality surfaces. To achieve this goal the first step was to produce single crystals as well as to do a complete characterization of their physical properties.

In addition, during the process of learning crystal growth, I prepared single crystals of LSCO. Meanwhile, a new phenomenon was discovered in cuprates, where an energy gap appears along the Fermi surface diagonal. Being able to grow my own crystals, I prepared a crystal with a very specific composition in order to study the newly discovered "nodal gap" with ARPES and understand its relation to magnetism employing neutron scattering and μSR.

Chapter 2

Experimental Methods

2.1 Traveling Floating Zone Technique

Crystal growth using the traveling floating zone technique (TFZ) has been extensively used to grow a variety of bulk crystals. Especially, crystals of metal oxides, such as the high-T_c cuprates. Large, high quality single crystal enables more reliable measurement of physical properties. In particular, when employing surface sensitive or direction dependent techniques. The TFZ method became very popular for growth of high T_c cuprates research, mainly because the cuprates melt incongruently. Namely, after melting, cuprates decompose into other phases upon solidification. Therefore, crystal growth methods which rely on crystallization from self melt, are rendered useless for cuprates. A solution to this problem, is ”solution growth” which have been developed to grow crystals of cuprates.The TFZ is a solution growth method, which also allows a high degree of control over the crystal growth process.[27]

2.1.1 The Image furnace

The basic concepts of an image furnace is the focusing of light, produced by high intensity xenon lamps by ellipsoidal or parabolic mirrors into a small volume of space ($\sim 1\ \mathrm{cm}^3$). A pressed polycrystalline feed rod is fed into the hot zone where the focused power creates a liquid molten zone. Figure 2.1 presents a schematic view of the image furnace core makeup of the furnace. The feed and seed rods are set within a quartz tube, where they are mounted on vertical shafts which can be rotated at variable speeds

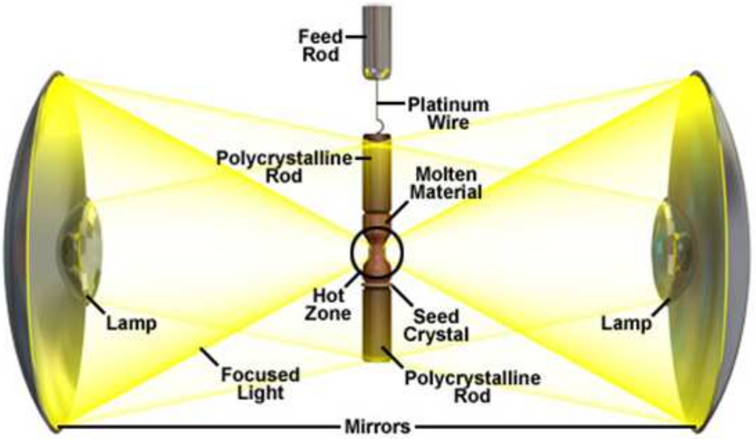

FIGURE 2.1: The inner core parts of the floating zone image furnace.

in different directions . The quartz tube allows crystal growth under either high gas pressure atmosphere of Argon, Nitrogen Oxygen, or vacuum if required. The top and bottom of the rods are placed at the common focal point (hot zone), where temperatures up to 3000^{o}C could be achieved. The maximum temperature depends mainly on the sample absorption, lamp power, pressure and atmosphere. The rods are meted and fused together by a molten zone. By raising the mirrors, the hot zone is passed trough the feed rod at a certain speed which determines the crystallization rate. Upon exiting the hot zone, The melt is solidified at the bottom of the seed rod producing a single crystal. An example of this process is shown in Fig 2.2.

2.1.2 Key Process Parameters in Crystal Growth

For successful growing crystals with TFZ method, one must control a vast range of growth conditions. Nonetheless there are some parameters which play a more significant role than others. There are four key parameters for crystal growth: A high quality feed rod, the Crystallization rate or "growth speed", atmosphere and the temperature at the molten zone.

High quality feed rod

The preparation of a feed rod is the initial stage of crystal growth using the TFZ method. For feed rods made from compacted powder, as most metal oxides do, excess porosity can undermine the stability of the molten zone due to liquid penetrating into the feed rod.

This is attributed to the capillary effect in which the melt is partially absorbed by the cavities between the fine particles in the feed rod. For most materials, the porosity can be reduced by either increasing the pressure at which the rod is compacted or sintering the feed rod at temperatures near its melting point prior to loading it to the image furnace. Therefore a uniform feed rod should be as close as possible to final crystal density, have a constant diameter and homogeneous composition. These factors are critical in order to achieve a stable molten zone for growing high quality single crystals.

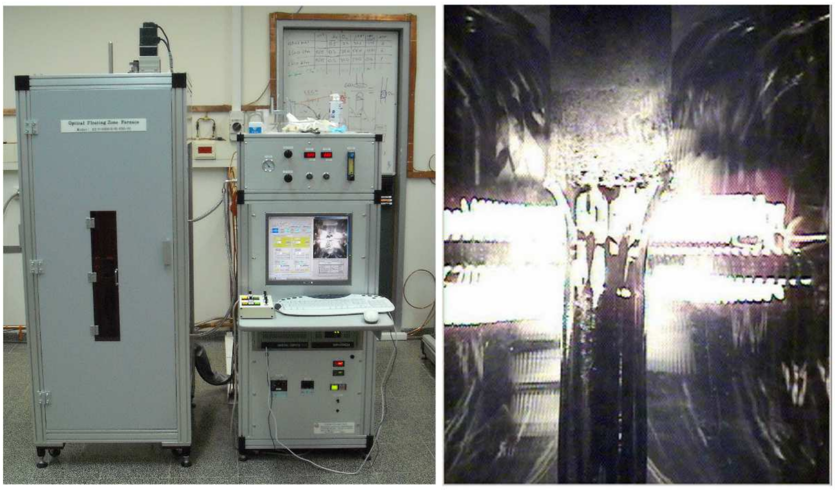

Figure 2.2: (LH) The floating zone furnace at work. (RH)Feed and seed rod are connected with a molten zone in between during crystal growth.

Crystallization rate (growth speed)

The growth speed or crystallization rate is unarguably one of the most critical parameter governing crystal quality when using the floating zone technique. Crystallization rate can strongly vary from 240 mm/h (GaAs) to 0.05 mm/h (Bi-based superconductors).It has been widely reported that changing growth speed can affect the grown crystal in terms of size, formation of bubbles, cracks, chemical composition, crystal alignment, twin formation and has a great influence on the solid-liquid interface and molten zone stability. The growth rate is mainly restricted by the slow solution diffusion process at the solid-liquid interface boundary, thus the typical growth rate required for optimal crystal quality depends on whether materials melt congruently or incongruently. For congruently melting materials, the molten zone and feed rod have equal composition, thus crystallization process is less limited by slow diffusion processes and relatively higher growth speed can be achieved. As for incongruently melting material, the melt composition differs from the original solid. Consequently, the compositional differences between the liquid and solid require solution diffusion at the solid-liquid interface, which is a significantly slower process, greatly reducing the crystal growth speed.

Growth atmosphere and gas pressure

Both atmosphere and gas pressure are crucial parameters when growing crystal in the TFZ method and play a key role in successful crystal growth. Both parameters are fairly easily controlled during the process, by selecting the right gas mixture coming in, and the desire pressure leaving the quartz tube. The main reason quoted for growing in higher than atmospheric pressure is to reduce the vaporization of volatile components from the sample. Reduction of evaporation losses is advantageous for the growth stoichiometric single crystals. The atmosphere can greatly differ composition between different materials. Typically for oxides, the atmosphere must contain Oxygen, anywhere between $0.01 - 10\%$, usually mixed with and inert gas such as Argon.

Lamp power and the temperature of the molten zone

The ”right” power level depends mainly on the chemical properties of the grown material, but is also affected by factors such as gas content and pressure, growth rate ,density and diameter of the feed rod ,lamp focus and the temperature gradient around the molten zone. For incongruently melting materials it is extremely important to adjust the power level according to the material’s phase diagram, which must remain constant when the right molten zone composition is achieved. Failing to fulfill this condition will result in either secondary phases or completely wrong chemical composition of the grown crystal.

2.2 Moun Spin Rotation (μSR)

Muon spin rotation, relaxation or resonance (μSR) is an experimental technique used for studying magnetic properties in condensed matter physics. This technique can directly measure the time dependence of the muons spin, after injecting it into the sample. With, μSR, static magnetic fields in the range of $10^{-5} - 1$ Tesla or magnetic field fluctuations on the time scale of $10^{-3} - 10^{-11}$ sec can be detected. Muons are short-lived subatomic particle of the lepton family with an electric charge (e^+ or e^-) and spin 1/2.

2.2.1 Principle of μSR

The production of muons is achieved by using high energy proton beams produced in cyclotrons. The protons are fired ontos a target to produce pions via

$$p + p \rightarrow \pi^+ + p + n$$

and then decay into muons via

$$\pi^+ \rightarrow \mu^+ + \nu_\mu$$

The decaying pions live on the target surface and have zero momentum, so the outgoing moun and neutrino leave with opposite momenta. The pions are spin-less particles, thus by angular momentum conservation the muon and neutrino must have opposite spins. The neutrino have a definite chirality so its spin must always be aligned or anti-aligned with its momentum, implying that the muons produced in this process must be 100% spins polarized. The muons are transported through the beam-line using a system of magnets, that conserve spin polarization. They hit the sample with an energy of 4MeV, where they lose their energy via scattering processes which has no effect on the muon's spin (usually Coulombic), leaving the spins polarized in a certain direction.

In the presence of external or internal magnetic field the muon spin begins rotation with an angular frequency of $\omega_\mu = \gamma_\mu B$, where γ_μ, the gyro-magnetic ratio is 1.355MHz/Tesla. The life time of the muon is $\tau_\mu = 2.2\mu s$, it decays in a three body process

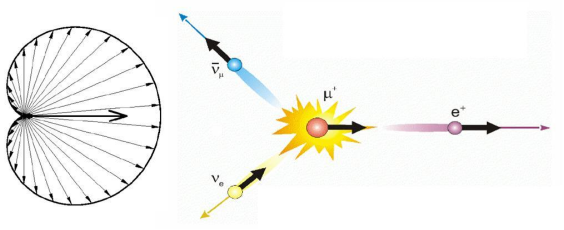

FIGURE 2.3: The angular distribution of emitted positrons.

$$\mu^+ \rightarrow e^+ + \nu_e + \bar{\nu_e}$$

This means that when placed in magnetic fields of few Tesla, typical for magnetically ordered materials, the muon spin will complete several revolution before decaying into a positron. The angular distribution of the emitted positrons is shown in Fig 2.3. The decay involves the weak interaction which violates parity, and leads to the positron being emitted preferentially along the direction of the muons spin after it decays. This effect allows one to measure the polarization of precessing muons.

2.2.2 The μSR experiment

A schematic diagram basics concept of a μSR experiment is shown in Figure 2.4. Once a muon is implanted in the sample, a clock start running and stops only when a positron is detected, using an array of plastic scintillators connected photo-multipliers surrounding the sample. In the simplest setup we have two detectors, the detector in the incident direction of the muon named the "forward" (denoted as F in the sketch) detector and the "backward" detector in the opposite (B in the sketch) direction.

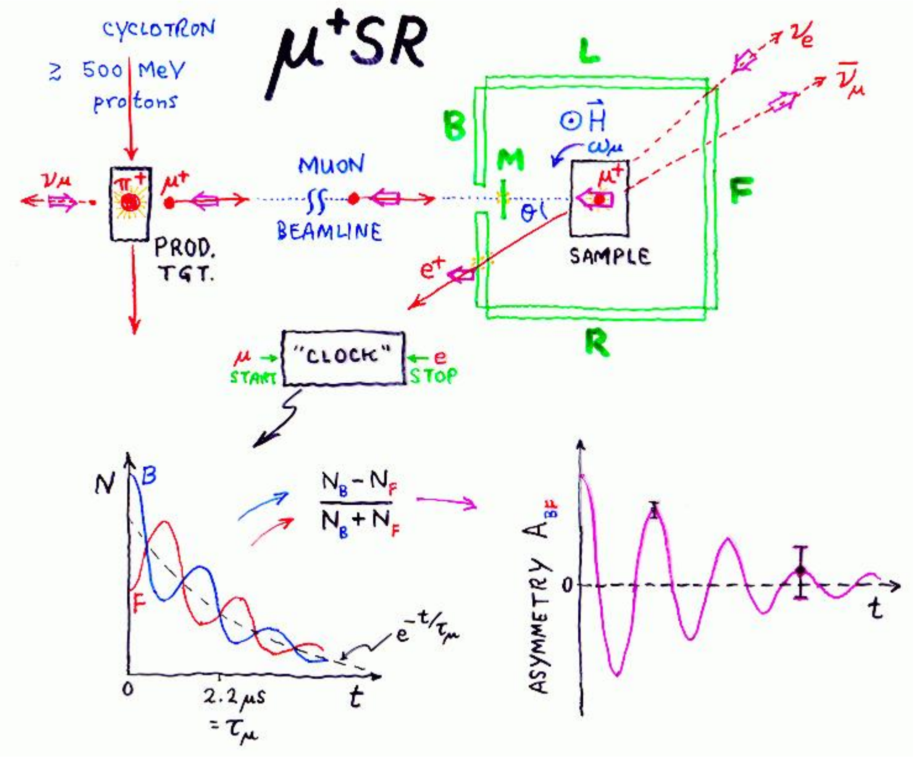

Figure 2.4: The Schematics of the μSR experiment.

In principle there could be up to six detector including, the right, left, top and bottom directions. A histogram of decay times is collected from each detector (N_F and N_B). The number of positrons detected in all the detectors decays exponentially with time, but if the muon "feel" a magnetic field the histogram will oscillate with the frequency ω_μ. The muon polarization can be extracted from the normalized difference between the histograms of the forward and backward detectors.

$$A\left(t\right)=\frac{N_F\left(t\right)-N_B\left(t\right)}{N_F\left(t\right)+N_B\left(t\right)}$$

A(t) is known as the asymmetry. It contains information about the local magnetic environment in materials, and is usually measured as a function of temperature. When

μSR can be performed with no external field, the muon will precess and reveal the internal field distribution, this is known as Zero Field **SR** (ZF-μSR) and it is useful in research of ferromagnets, anti-ferromagnets and spin-glasses. μSR can be also carried out when applying an external magnetic field. There are two different configurations for μSR in external field: longitudinal field μSR, in which the initial muon spin polarization is parallel to the applied field direction and transverse field μSR, in which the initial muon spin polarization is perpendicular to the applied field direction.

2.3 Neutron Scattering

Neutron scattering is a versatile technique, which is particularly well suited to studying strongly correlated electron systems. This is due in large part, to the basic properties of neutrons, combined with technology that allows production and delivery of high neutron fluxes, combined with instrumentation designed specially for the study of condensed matter systems. The de-Broglie wave length of thermal neutron is in the order of inter-atomic distances (4 Å) allowing diffraction measurement possible to study the structure of solids. Moreover, the energy spectrum of thermal neutrons is in the same order of many condensed matter excitations (phonons, magnons, etc.). Inelastic scattering processes which excite the system, have a large relative shift in the neutron energies, and so are an accurate method of measuring the excitation spectrum of a system.

Neutrons has several advantages over x-rays which are similarly used in condensed matter. First, neutrons have a magnetic moment, thus can interact with the dipole moments of electrons and ions, allowing neutron scattering to directly probe the magnetic order, as well as excitations in condensed matter systems. In addition, the probability to scatter an x-ray photon of an atom, is proportional to the number of electrons, while neutron scattering amplitude form atom varies randomly across the periodic table. Therefore, neutrons are able to "see" light atoms, oxygen for example, in compounds which also contain heavy atoms. Finally, neutrons scatter weakly, allowing them to penetrate several centimeters into the sample serving more as a bulk probe, in contrast to x-ray which serves as more surface sensitive techniques. This can also be a disadvantage as it requires large crystals in order to obtain statistically sound results.

2.3.1 Elastic Neutron Scattering

The principle aim of a neutron scattering experiment is to determine the probability of a neutron, which is incident on the sample with an initial wave-vector $\mathbf{k}_i$, to be scattered into a final state with a wave-vector $\mathbf{k}_f$. The angle between $\mathbf{k}_i$ and $\mathbf{k}_f$ is often labeled as

2θ. The intensity of scattered neutrons is measured as a function of momentum transfer to the sample, $\hbar\mathbf{Q}$, where $\mathbf{Q}$ is known as the *scattering vector* and is defined as

$$\mathbf{Q} = (\mathbf{k}_i - \mathbf{k}_f) \tag{2.1}$$

The corresponding energy transfer is given by

$$\hbar\omega = \frac{\hbar^2}{2m}\left(\mathbf{k}_i^2 - \mathbf{k}_f^2\right) \tag{2.2}$$

The three vectors $(\mathbf{k}_i, \mathbf{k}_f, \mathbf{Q})$ together form the scattering triangle which is shown in Fig. 2.5. Eqs 2.1 and 2.2 describe the momentum and energy conservation of a neutron scattering process, respectively. For $\mathbf{k}_i = \mathbf{k}_f$ we have $\hbar\omega = 0$, i.e, elastic scattering. In the case of, $\mathbf{Q} = \mathbf{G}$, where $\mathbf{G}$ is a reciprocal lattice vector, we satisfy the condition known as Bragg's law (coherent elastic scattering). If $\mathbf{Q}$ does not coincide with a reciprocal lattice vector $\mathbf{G}$ and $\hbar\omega \neq 0$, the neutron scatters inelastically. For inelastic processes, the scattering vector can be decomposed according to $\mathbf{Q} = \mathbf{G} + \mathbf{q}$. where $\mathbf{q}$ is the wave vector of an elementary excitation. Neutron scattering turns out to be the most precise technique for measuring the dispersion relation $\hbar\omega(\mathbf{q})$ across the reciprocal space.

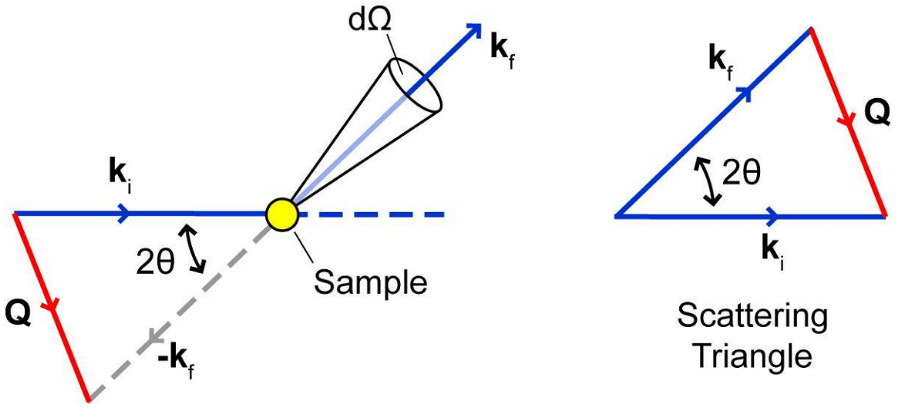

FIGURE 2.5: Schematic diagram of the geometry of a neutron scattering experiment. Incident neutrons with wave-vector $\mathbf{k}_i$ are scattered by the sample into a final state $\mathbf{k}_f$. The scattering triangle defines the scattering wave-vector $\mathbf{Q} = \mathbf{k}_i - \mathbf{k}_f$. $d\Omega$ is the unit of solid angle subtended by the detector.

2.3.2 Neutron Scattering cross-section

The neutron partial differential scattering cross-section corresponds to a number of neutrons scattered per unit time into a small solid angle dΩ, around the outgoing wave vector $\mathbf{k}_f$, with energy transfer between $\hbar\omega$ and $\hbar\left(\omega + d\omega\right)$ divided by the flux of the incident neutrons determined by the incoming wave vector$\mathbf{k}_fi$. To obtain an expression for the partial differential cross-section we consider the probability of transition of a neutron-sample system from an initial sample state λ_i to a final sample state λ_f. Since the neutron scattering can be considered as a very weak process, the interaction potential between neutron and sample can be treated as a perturbation and Fermi golden rule can be applied to calculate the transition probability. The theoretical expression for the cross section, after summation of all possible initial and final sample state of the system, and over all possible initial and final spin state, (σ_i, σ_f) of the neutron can be written as

$$\frac{\partial^2\sigma}{\partial\Omega\partial E_f} = \frac{k_f}{k_i}\left(\frac{m_n}{2\pi\hbar^2}\right)^2 \sum_{\sigma_i,\sigma_f} p_{\sigma_i} \sum_{\lambda_i,\lambda_f} p_{\lambda_i} |\langle\sigma_f\lambda_f \left|V\left(\mathbf{Q}\right)\right| \sigma_i\lambda_i\rangle|^2 \delta\left(E_{\lambda_f} - E_{\lambda_i} - \hbar\omega\right) \quad (2.3)$$

Where $V(\mathbf{Q})$ is given by the Fourier transform of the neutron-system interaction potential $V(\mathbf{r})$:

$$V\left(\mathbf{Q}\right) = \int V\left(\mathbf{r}\right) \exp\left(i\mathbf{Q}\cdot\mathbf{r}\right) d^3\mathbf{r} \quad (2.4)$$

The scattering cross-section is therefore dependent on the type of interaction between the neutron and the matter it scatters from, or in other words, the interaction potential $V(\mathbf{r})$). The derivations of this potential and the corresponding scattering cross-sections for different interactions are covered in depth by textbooks as Squires and others [28].

2.4 Angle Resolved Photoemission Spectroscopy

The photoemission phenomena was discovered by H. Hertz in 1887 and then explained by Einstein in 1905. The effect of photoemission refers to the fact that a metal exposed to light will emit a current of electrons. Einstein gave his noble-winning relation for the energetic balance of photoemission

$$E_k = h\nu - \phi - |E_B(\mathbf{k})| \tag{2.5}$$

Where E_k is the kinetic energy of the emitted electron , $h\nu$ is the photon energy, $|E_B(\mathbf{k})$ is the binding energy and ϕ is the work function of the material.

In Angle Resolved Photoemission Spectroscopy (ARPES) experiments, a photoemitted electron current is collected as function of energies and angles. ARPES essentially measures the probability to remove an electron with a specific energy and momentum form a sample. The intensity $I\left(k,\omega\right)$ is given by:

$$I\left(k,\omega\right) = I_0 M\left(k\right) f\left(\omega\right) A\left(k,\omega\right) \tag{2.6}$$

where $M\left(k\right)$ is the matrix element of the electron-photon interaction, $f\left(\omega\right)$ is the Fermi-Dirac distribution and $A\left(k,\omega\right)$ is the single electron spectral function. $A\left(k,\omega\right)$ can be related to the self-energy of the system $\Sigma = \Sigma' + i\Sigma$”:

$$A\left(k,\omega\right) = -\frac{1}{\pi}\frac{\Sigma''\left(k,\omega\right)}{\left[\omega - \epsilon_k - \Sigma'\left(k,\omega\right)\right]^2 + \left[\Sigma''\left(k,\omega\right)\right]^2} \tag{2.7}$$

The spectral function $A\left(k,\omega\right)$ holds full information about the electronic structure of the sample, from the band-structure, to the deep core-level electrons and up to the Fermi surface geometry. Any correlation gap, re-normalization of the dispersion, or interaction with a phonon or magnon will be apparent in the spectral function. For non-interacting systems, $A\left(k,\omega\right)$ is consisted from a set of δ-functions that define the electronic dispersion and band-structure of the material. In the presence of interactions, δ-functions are replaced by combination of an incoherent broad features and a sharp quasi-particle peak, ARPES, provides information about the electronic structure of materials in a momentum-resolved manner.

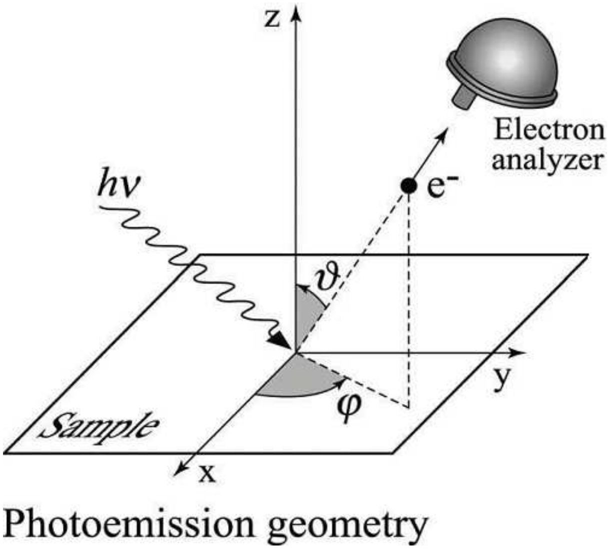

FIGURE 2.6: The geometry of the ARPES experiment. By measuring the angle of the emitted electrons relative to the sample normal and to the detector axis, the momentum of the electrons in the initial state can be calculated.

Because the electrons travel a macroscopic distance (∼1m) before entering the analyzer they can be treated as free electrons. In the free electron-approximation the total momentum of a photoemitted electron is given by

$$|p| = \frac{\sqrt{2mE_{kin}}}{\hbar} \tag{2.8}$$

On the sample surface, the parallel component of the electron momentum is required to be conserved. So for electrons which are transmitted through the surface the parallel momentum is:

$$\left|p_{||}\right| = \left|k_{||} + G_{||}\right| = \frac{\sqrt{2mE_{kin}}}{\hbar} \sin\theta \tag{2.9}$$

where **G** is a reciprocal lattice vector, **k** is the crystal momentum in first Brillouin zone and θ is the angle between the outgoing electron and normal to the surface (see Fig. 2.6). Therefore, by knowing the takeoff angles of the electron relative to the crystal axes and the detector (see Fig. 2.6), the momentum wavevector of the out coming photoelectron can be calculated. From momentum conservation, the initial state momentum of the electrons can be calculated. Figure 2.7 demonstrates simulated raw ARPES data. The data can be interpreted as Lorentzians in $\mathbf{k}$ and E around $\mathbf{k}_{\|}$ and $\varepsilon\left(\mathbf{k}_{\|)}\right)$ which is following the bulk electronic dispersion relation. The width of Lorentzians is proportional to the life time and correlation length or mean-free path of the quasi-particles.

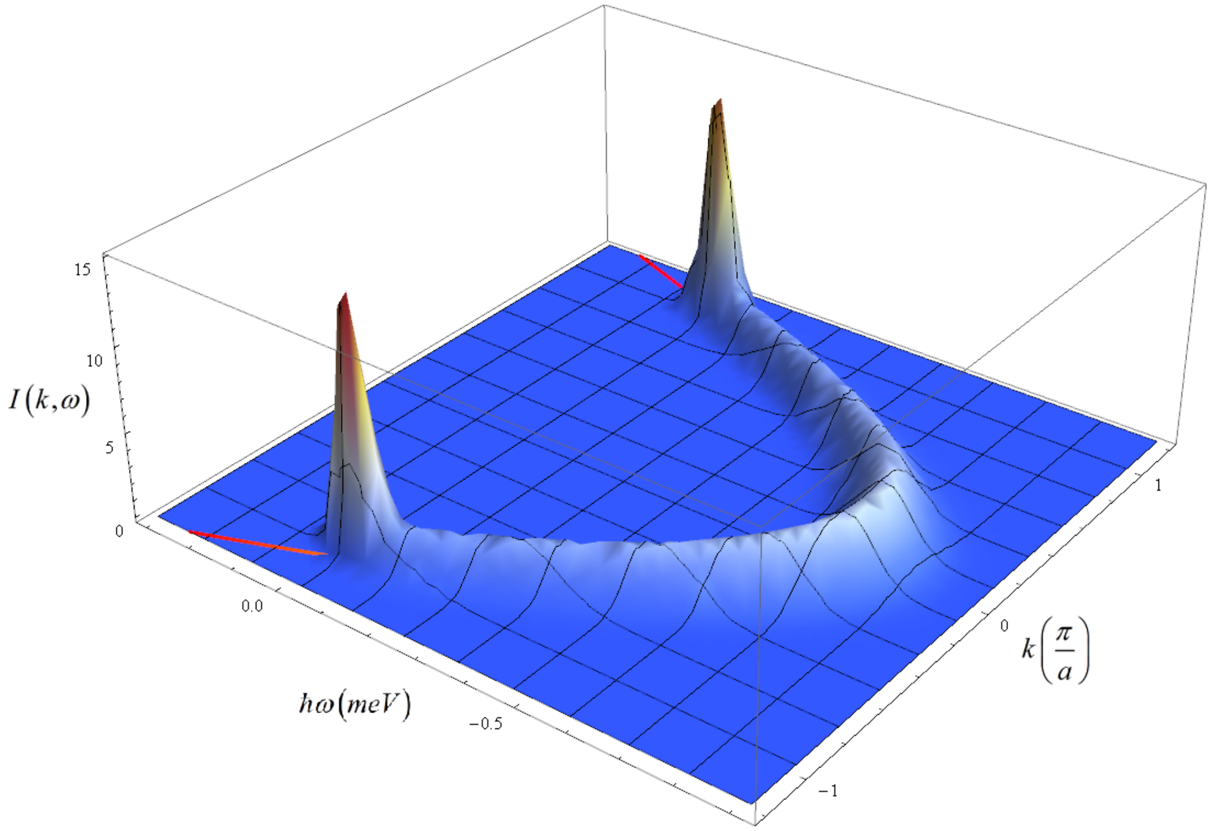

FIGURE 2.7: An illustration of the data recorded in an ARPES experiment along a nodal cut, in the (π, π) direction. A ridge made of Lorentzian around $\mathbf{k}_{\|}$ and $E\left(\mathbf{k}_{\|)}\right)$ following the dispersion relation calculated using a Tight Binding model, with quasi-particle peak close to E_f.

Chapter 3

Results (as published articles)

J Supercond Nov Magn (2012) 25:2331–2335
DOI 10.1007/s10948-012-1669-z

ORIGINAL PAPER

New Perspectives for Cuprate Research: $(Ca_xLa_{1-x})(Ba_{1.75-x}La_{0.25+x})Cu_3O_y$ Single Crystals

**Gil Drachuck · Meni Shay · Galina Bazalitsky · Rinat Ofer · Zaher Salman ·
Alex Amato · Christof Niedermayer · Dirk Wulferding · Peter Lemmens · Amit Keren**

Received: 25 March 2012 / Accepted: 22 May 2012 / Published online: 6 June 2012
© Springer Science+Business Media, LLC 2012

Abstract We report the successful growth of a large $(Ca_xLa_{1-x})(Ba_{1.75-x}La_{0.25+x})Cu_3O_y$ (CLBLCO) single crystal. In this material, x controls the maximum of T_c (T_c^{max}), with minimal structural changes. Therefore, it allows a search for correlations between material properties and T_c^{max}. We demonstrate that the crystals are good enough for neutron scattering and cleave well enough for Raman scattering. These results open new possibilities for cuprate research.

Keywords Crystal growth · Superconductivity · Magnetism

Although high quality single crystals of cuprate superconductors have been available for quite some time, comparing the properties of different crystals often raised more questions than answers. The main problem is that many parameters differ between various cuprates simultaneously, and it is difficult to understand which material property is responsible for which physical property. A proper understanding of cuprate superconductivity can emerge only when it is possible to vary the material parameters one at a time preferably in single crystals. Here, we describe the growth and characterization of large single crystals of a $(Ca_xLa_{1-x})(Ba_{1.75-x}La_{0.25+x})Cu_3O_y$ (CLBLCO) superconductor, in which it was previously demonstrated that the variable x changes only the Cu–O–Cu buckling angle and bond distance, and hence the super-exchange [1]. We also demonstrate that experiments such as neutron scattering, Raman scattering, and more can be performed on these crystals.

The phase diagram of CLBLCO for various values of x and y is presented in Fig. 1(a) [2]. When varying x, the amount of Lanthanum in the chemical formula remains constant and, therefore, x stands for the Calcium-to-Barium ratio. The parameter y controls the oxygen level and moves the system between the different phases. At around $y = 7.15$, each family has its maximum T_c [T_c^{max}]. Changing x from 0.1 to 0.4 varies T_c^{max} from 58 K to 80 K [3, 4]; roughly a 30 % increase. This T_c^{max} variation is achieved with no apparent structural changes.

All CLBLCO compounds have YBCO-like structure with two CuO_2 planes and two disordered "chain" layers per unit cell. The symmetry is tetragonal for all values of x and y [5]. The level of disorder is also similar for all families [6]. Therefore, a priori, there is no reason for T_c^{max} to depend on x. However, increasing x increases the amount of the Ca^{2+} in the Y site of YBCO at the expense of La^{3+}. This charge transfer is equivalent to reducing the positive charge on the (YBCO) Y site and increasing it on the (YBCO) Ba site, and could alter the Cu–O–Cu buckling angle. In-

G. Drachuck (✉) · G. Bazalitsky · R. Ofer · A. Keren
Department of Physics, Technion—Israel Institute of Technology,
Haifa 32000, Israel
e-mail: gil.drchk@gmail.com

M. Shay
Department of Physics and Optical Engineering, Ort Braude
College, P.O. Box 78, 21982 Karmiel, Israel

Z. Salman · A. Amato
Laboratory for Muon Spectroscopy, Paul Scherrer Institute,
5232 Villigen PSI, Switzerland

C. Niedermayer
Laboratory for Neutron Scattering, Paul Scherrer Institute,
5232 Villigen PSI, Switzerland

D. Wulferding · P. Lemmens
Institute for Condensed Matter Physics, TU Braunschweig,
38106 Braunschweig, Germany

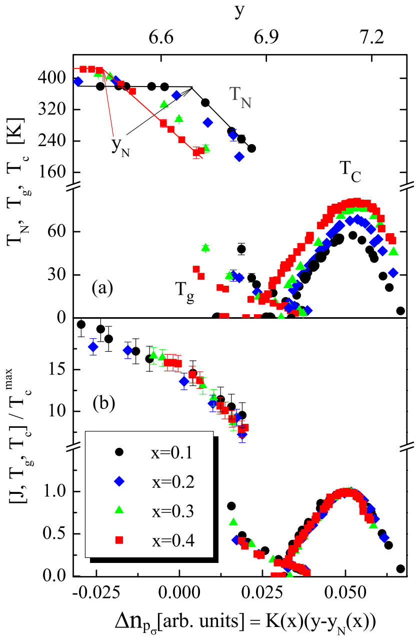

Fig. 1 (**a**) The phase diagram of CLBLCO showing the Néel (T_N), glass (T_g) and superconducting (T_c) temperatures over the full doping range for the four families. y_N indicates the oxygen level where T_N start to drop. (**b**) The unified phase diagram of CLBLCO. The critical temperatures, and J extracted from T_N, are divided by $T_c^{\max}$ and plotted as a function of doping variation in the oxygen orbital Δn_{p_σ}

deed, it was found by high resolution neutron diffraction that as x increases the Cu–O–Cu bond becomes shorter and straighter [1], while other structural properties remain intact [6]. The bond length and buckling are the major factors that control the orbital overlap and, in turn, the hopping parameter t or the super-exchange J. Thus, the newly grown CLBLCO crystal can shed new light on the impact of t or J on properties such as: $T_c^{\max}$, the structure of the Fermi surface, the magnetic resonance, the size of the gap/pseudogap, and more.

For example, early muon spin rotation (μSR) measurements using compressed CLBLCO powder samples in the anti-ferromagnetic phase, combined with theoretical calculations, revealed that J is x-dependent, as expected, and that $T_c^{\max}(x) \propto J(x)$ [7]. Similarly, NMR established that simple valence counting does not represent the true doping of the CuO$_2$ planes and that a doping efficiency parameter $K(x)$ should be introduced; the number of holes in the oxygen 2p$_\sigma$ orbital is given by $\Delta n_{2p} = K(x)(y - y_N)$ where y_N is defined in Fig. 1(a) [2]. Interestingly, when plotting $J(x)$, T_g, and T_c normalized by $T_c^{\max}(x)$ as a function of Δn_{2p} a unified phase diagram is generated, as depicted in Fig. 1(b) [2, 7].

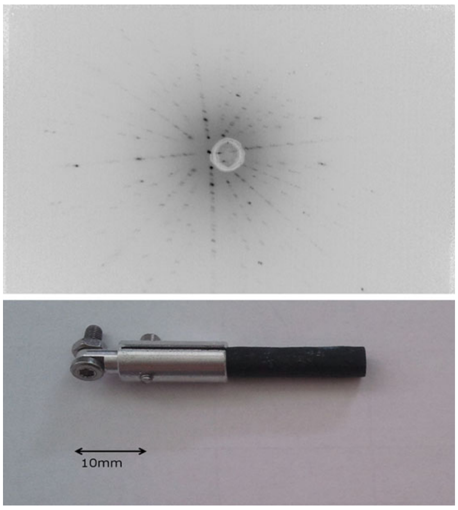

Fig. 2 (*Top*) Laue diffraction pattern of the (001) crystal plane taken from the CLBLCO crystal. (*Bottom*) Photograph of the grown CLBLCO Crystal

However, μSR is not a direct probe of J, and more profound work is needed to clarify the relation between the superconducting and magnetic energy scales. Inelastic neutron or Raman scattering are more appropriate for direct J determination. Equally, NMR does not measure the Fermi surface size directly and a proper ARPES measurement is needed. These advanced measurements require large single crystals with specific orientation or high quality surfaces. Here, we report the production of such crystals by the Traveling Solvent Floating Zone method. Details of the growth and characterization are given in the Appendix. An optical image and a Laue diffraction pattern of one of the crystals are shown in Fig. 2. We also demonstrate the applicability of several experimental techniques to these crystals. It should be pointed out that small crystals were grown before but only their chemical properties where analyzed [8–10].

The bulk superconducting properties of this crystal were tested by transport and magnetization measurements. The $x = 0.1$ and 0.4 crystals are cut into a rectangular shape and post-annealed in oxygen to achieve optimal doping. The $x = 0.1$ is annealed at a temperature of 300 °C and ambient pressure for 150 hr. The $x = 0.4$ is annealed at a temperature of 400 °C and a pressure of 65 bar for 90 hr. Figure 3 shows normalized resistivity and normalized susceptibility. We found that $T_c = 58$ and 78 K for $x = 0.1$ and 0.4, respectively, which is in perfect agreement with powder sample measurements. T_c is defined as the temperature where the resistivity vanishes upon cooling or the susceptibility vanishes upon warming. The transition into the superconducting state of the $x = 0.1$ crystal is wide. It spans 10 K in the susceptibility measurement and 25 K in the resistivity

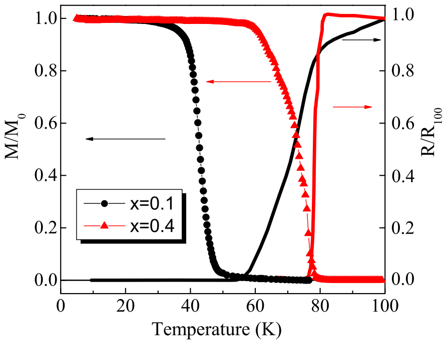

Fig. 3 Normalized resistivity and susceptibility as a function of T obtained from an optimally doped crystal with $x = 0.1$ and $x = 0.4$

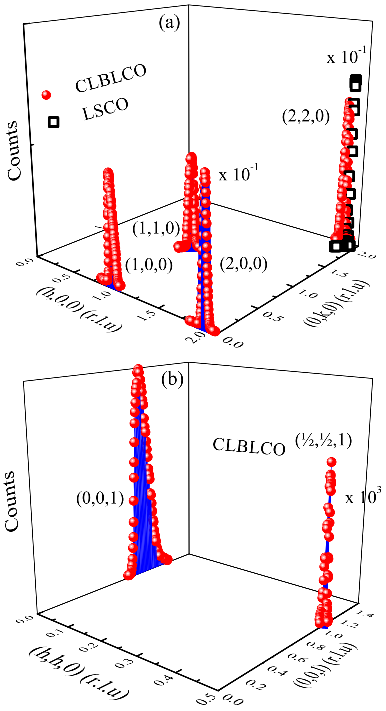

Fig. 4 (**a**) The structural Bragg peaks (*red circles*) of the CLBLCO $x = 0.1$ single crystal obtained by neutron scattering. The (200) peak intensity is divided by 10 for clarity. The empty *black squares* described the (020) peak measure on a LSCO crystal as a reference. (**b**) The magnetic Bragg peak $(\frac{1}{2}\frac{1}{2}1)$ multiplied by 10^3 for clarity, and the structural peak (001) (Color figure online)

measurement. This is probably due to very small traces of high x values. The transition of the $x = 0.4$ crystal is sharp in both susceptibility and resistivity measurements. Nevertheless, there are clear variations in T_c between optimally doped crystal with different x values. The superconducting volume fraction extracted from the magnetization measurement is approximately 100 %.

The most demanding requirements from single crystals are those of the neutron scattering experimental technique. For this technique, the crystals must be of the order of 10 gr. To check the applicability of neutron scattering to our crystal, we use the ORION beam-line at PSI, Switzerland. This beam-line provides neutrons with a wavelength of $\lambda = 2.22$ Å. The crystal is kept at room temperature. Using an $(h, k, 0)$ scan and the YBCO structure parameters taken from ISCD's "Lazy Pulverix" website, we detect the (100), (200), (110), (220) nuclear Bragg peaks as presented in Fig. 4(a). For comparing crystal qualities, we also present the strongest LSCO nuclear Bragg peak, namely, the (220) from a sample of equal size. The intensity of the strongest LSCO peak, (2, 2, 0), and the strongest CLBLCO peak, (2, 0, 0), is similar.

In Fig 4(b), we show neutron scattering data acquired on the MORPHEUS beam-line. This beam line has a higher flux and a wavelength of $\lambda = 5.02$ Å which enables us access to the first allowed magnetic Bragg peak of CLBLCO. Indeed, using an (h, h, l) scan we are able to detect the nuclear (001) and the magnetic $(\frac{1}{2}\frac{1}{2}1)$ Bragg peaks of our CLBLCO crystal as well. The magnetic peak intensity in the figure is multiplied by 10^3 for clarity.

We also check the major magnetic properties of our crystal by performing a ZF-μSR experiment, at PSI, Switzerland. Figure 5(a) shows the μSR asymmetry data of an $x = 0.1$ crystal by symbols, and the fit of the function

$$Asy(t) = \sum_{i=0}^{2} A_i \exp(-\lambda_i t)\cos(\omega_i t + \phi) + B_g \qquad (1)$$

to the data by solid lines. Here, ω_0 is fixed at 0, and ω_1 and ω_2 stand for high and low frequencies, respectively. The two frequencies extracted from the fit are presented in Fig. 5(b). They result from two different muon sites, common to most cuprates. Above 300 K, the two frequencies merge into one. The Néel temperature is determined from the $\omega \to 0$ limit giving $T_N = 375$ K, which is the same as the $x = 0.1$ powder sample.

For a variety of experimental techniques having single crystals is insufficient; these crystals must also cleave with high quality exposed surfaces. To test this requirement, we cleave one of our samples and examine the surface by a scanning electron microscope (SEM) equipped with an electron backscatter diffraction module (EBSD). A SEM micrograph taken at an acceleration voltage of 25 kV is shown in the inset of Fig. 6. A 100 × 200 μm^2 crystal facet is clearly visible. The EBSD diffraction patterns from one point on the surface is shown in Fig. 6. Clear Kikuchi lines can be seen in the diffraction [11]. A fit to the expected Kikuchi lines from the YBCO structure is also presented. The patterns reveal that the surface of the facet is perpendicular to the crystal

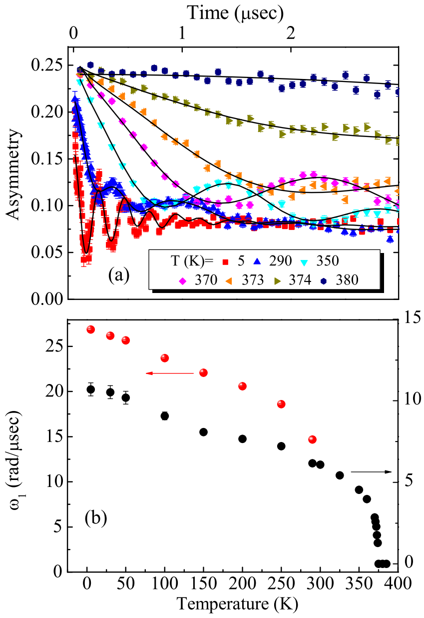

Fig. 5 (**a**) μSR Asymmetry with a fit of Eq. (1) to the data at various temperatures. (**b**) Muon spin oscillation at high frequency ω_1 (*red*) and low frequency ω_2 (*black*) as a function of temperature from the CLBLCO $x = 0.1$ crystal (Color figure online)

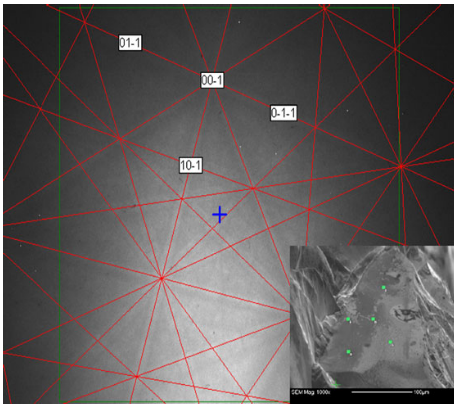

Fig. 6 *Main panel*: The EBSD diffraction pattern consisting of intersecting Kikuchi lines, where the *red lines* depict the most probable fit to the YBCO structure. *Inset*: SEM micrograph of the CLBLCO crystal showing a large facet. The *green squares* identifies the spots at which EBSD patterns were acquired (Color figure online)

c-axis. We repeat the EBSD measurements at all the (green) points in the inset, and find the same Kikuchi pattern. This indicates that all points share the same crystal orientation and that the surface is perpendicular to the crystallographic c-axis. This finding is also confirmed by the Raman scattering experiment described below.

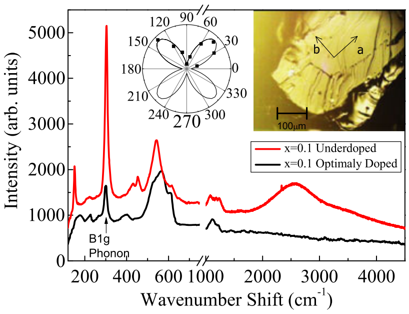

Fig. 7 *Main panel*: Unpolarized Raman spectra of the underdoped crystal (*red*) and the optimally doped crystal (*black*); note the change of scale at the axis breaker. The optical phonons are in the range 100–600 cm^{-1}. The broad two-magnon peak is at 2500 cm^{-1}. This peak exists only in the underdoped crystal, as expected. *Left inset*: The intensity of the B$_{1g}$ phonon as a function of the angle between the incident polarization and the crystal a-axis using polarizer and analyzer at 90° to the polarizer. This shows the 4-fold symmetry of the crystal and determines its orientation. *Right inset*: The cleaved crystal facet and the crystal axis as determined using the B$_{1g}$ phonon

Raman spectra of an under and optimally doped CLBLCO samples are shown in Fig. 7. The samples are freshly cleaved and cooled in an evacuated cryostat to $T = 20$ K. One surface is shown in the inset of Fig. 7. The spectra are obtained by a Jobin-Yvon micro-Raman spectrometer (LabRam-HR 800) with a $\lambda = 532$ nm solid state laser and a power of less than 1 mW to avoid overheating. The laser is focused by a microscope objective lens with ×50 magnification to a spot of about 10 μm diameter. The scattered light is collected in backscattering geometry and dispersed by a diffraction grating with 1800 grooves/mm onto a liquid nitrogen cooled CCD array. Polarized Raman spectra are obtained with a Polaroid polarizer and analyzer placed after the laser and before the grating.

Since CLBLCO belongs to the tetragonal space group P$_{4/\mathrm{mmm}}$, symmetry analysis [12] yields $4\mathrm{A}_{1g} + 1\mathrm{B}_{1g} = 5$ Raman active optical phonons for scattering in the ab plane. In $a'(c,c)a'$ polarization (i.e., both polarizer and analyzer rotated by 45° from the crystallographic a axis), only A$_{1g}$ phonons are allowed, while in $a'(c,c)b'$ polarization (with the analyzer set perpendicular to the polarizer and 45° from the crystallographic b axis) only B$_{1g}$ phonons are allowed. In the underdoped crystal, four of the five phonons are clearly observed at 145, 298, 423, 446 cm^{-1}. The fifth optical phonon is either at 209 cm^{-1} where a very shallow peak is observed, or it overlaps with the multi-phonon peaks starting around 500 cm^{-1}. For comparison, YBCO$_6$ has five phonons [13, 14] at about 140, 230, 335, 435, 500 cm^{-1}.

Using the rotational anisotropy of the 298 cm^{-1} B_{1g} phonon with respect to the electric field, the a and b direction of the crystal are found. The center inset of Fig. 7 shows the phonon intensity as a function of the polarizer angle from a. The crystal direction are depicted on the cleave surface in Fig. 7.

Another feature of the underdoped crystal, common to all cuprates, is the broad peak centered at $\Delta E_{\max} = 2580(20)$ cm^{-1}. This peak is attributed to two-magnon scattering. The Heisenberg exchange constant J is roughly given by $\Delta E_{\max}/3 = 1240(10)$ K [15, 16]. This estimation is in good agreement with the µSR data given in Fig. 1(a) and (b); for the most underdoped $x = 0.1$ sample, we have $J/T_c^{\max} = 20.4(1.5)$ and $T_c^{\max} = 58$ K, giving $J = 1170(100)$ K. Achieving a better agreement between the two values requires further investigations. Finally, the two-magnon peak is absent from the spectrum of the optimally doped crystal due to an overdamping of the spin excitations, which is also depicted in Fig. 7; the spectra are shifted in intensity for clarity.

Our data indicate that CLBLCO can be grown as large single crystals. The crystals are large enough for neutron scattering. The crystals are cleavable, giving high quality surfaces, which make them suitable for surface probes. Within the realm of our experiments, the crystals have the same properties as the original powder. These properties, combined with the unique phase diagram of CLBLCO open new perspectives for cuprate research.

Acknowledgements One of us (A.K.) would like to thank John Tranquada and Genda Gu for a two month visit to their lab and excellent tutorial on single crystal growth, and to Kazimierz Conder and Ekaterina Pomjakushina for helpful discussion. This research was funded by the Israeli Science Foundation and the ESF.

Appendix

The crystals are grown using a Crystal System Corp. optical furnace (FZ-T-4000-H) equipped with four parabolic mirrors and 300 W lamps. CLBLCO powder is first prepared using solid state reaction from stoichiometric proportions of La_2O_3 (99.99 %), $CaCO_3$ (99.9 %), $BaCO_3$ (99.9 %), and CuO(99 %). The starting materials are mixed, calcined, and ground repeatedly at 900, 925, 950, 950 °C for 24 hours, then tested for impurities using XRD. The CLBLCO powder is then packed into rubber tubes and hydrostatically pressed at 400 MPa, producing 15–20 cm × ∅ 7 mm cylindrical rods. The density of the rods reaches more than 90 % after sintering them at 1040 °C for 24 hours ensuring stable uninterrupted growth. The growth is carried out at a rate of 0.35 mm/h in argon atmosphere with 0.05–0.1 % oxygen, with both feed and seed rotating in opposite directions at 15 rpm. The growth lasts up to 10 days resulting in 50–100 mm long crystals. The grown crystals are annealed in argon at 850 °C for 120 hours to relieve thermal stress, and, when needed, to remove excess oxygen for magnetic measurement (µSR and elastic neutron scattering). It is important to mention that we do not find any traces of copper on the furnace quartz tube as usually happens with LSCO growth. Therefore, we do not add any excess copper to the initial powder.

We also perform Inductively-coupled plasma atomic-emission spectroscopy (ICP-AES) [17] measurements on the crystals and the starting powders. For ICP, we prepare 10 test tubes with the 100 mg of crystal dissolved in “Trace Select” grade Nitric Acid, as well as 5 test tubes of the starting powder. ICP allows us to measure the molar ratio of Ca, Ba, and La to Cu in the mixture. Knowing that we have 3 Cu atoms per unit cell, we found $Ca = 0.102 \pm 0.005$, $Ba = 1.565 \pm 0.05$, and $La = 1.319 \pm 0.02$ atoms per unit cell in the powder case. The nominal values should be $Ca = 0.1$, $Ba = 1.65$, and $La = 1.25$. This sets the sensitivity of the ICP technique. For the crystal, we find that $Ca = 0.102 \pm 0.005$, $Ba = 1.57 \pm 0.02$, and $La = 1.295 \pm 0.006$ atoms per unit cell. Therefore, there is no difference in the Ca, Ba, or La content, between the crystals and powders within the accuracy of the measurement.

References

1. Ofer, R., Keren, A., Chmaissem, O., Amato, A.: Phys Rev. B **78**, 140508(R) (2008)
2. Amit, E., Keren, A.: Phys. Rev. B **82**, 172509 (2010)
3. Goldschmidt, D., Reisner, G.M., Direktovitch, Y., Knizhnik, A., Gartstein, E., Kimmel, G., Ecksteі, Y.: Phys. Rev. B, Condens. Matter Mater. Phys. **48**, 532 (1993)
4. Kniznik, A., Direktovich, Y., Reisner, G.M., Goldschmidt, D., Kuper, C.G., Eckstein, Y.: Physica C **321**, 199 (1999)
5. Keller-Berest, F., Megtert, S., Collin, G., Monod, P., Ribault, M.: Physica C **161**, 150 (1989)
6. Keren, A.: New J. Phys. **11**, 065006 (2009)
7. Ofer, R., Bazalitsky, G., Kanigel, A., Keren, A., Auerbach, A., Lord, J.S., Amato, A.: Phys. Rev. B **74**, 220508(R) (2006)
8. Noji, T., Akagawa, H., Oikawa, T., Ono, Y., Koike, Y.: J. Low Temp. Phys. **117**, 705 (1999)
9. Noji, T., Akagawa, H., Ono, Y., Koike, Y.: JLTP **131**, 699 (2003)
10. Chen, C., et al.: J. Mater. Sci., Mater. Electron. **10**, 581–584 (1999)
11. Maitland, T., Sitzman, S.: Scanning Microscopy for Nanotechnology pp. 41–75 (2007)
12. Kroumova, E., Aroyo, M.I., Perez Mato, J.M., Kirov, A., Capillas, C., Ivantchev, S., Wondratschek, H.: Phase Transit. **76**(1–2), 155–170 (2003)
13. Krol, D.M., Stavola, M., Weber, W., Schneemeyer, L.F., Waszczak, J.V., Zahurak, S.M., Kosinski, S.G.: Phys. Rev. B **36**, 8325 (1987)
14. Thomsen, C., Liu, R., Bauer, M., Wittlin, A., Genzel, L., Cardona, M., Schönherr, E., Bauhofer, W., König, W.: Solid State Commun. **65**, 55 (1988)
15. Weber, W.H., Ford, G.W.: Phys. Rev. B **40**, 6890 (1989)
16. Canali, C.M., Girvin, S.M.: Phys. Rev. B **45**, 7127 (1992)
17. Hill, S.J.: Inductively Coupled Plasma Spectrometry and its Applications, 2nd edn. (2007)

RAPID COMMUNICATIONS

PHYSICAL REVIEW B **89**, 121119(R) (2014)

Linking dynamic and thermodynamic properties of cuprates: An angle-resolved photoemission study of $(\mathrm{Ca}_x\mathrm{La}_{1-x})(\mathrm{Ba}_{1.75-x}\mathrm{La}_{0.25+x})\mathrm{Cu}_3\mathrm{O}_y$ ($x = 0.1$ and 0.4)

Gil Drachuck,[1] Elia Razzoli,[2] Rinat Ofer,[1] Galina Bazalitsky,[1] R. S. Dhaka,[2] Amit Kanigel,[1] Ming Shi,[2] and Amit Keren[1]
[1]*Department of Physics, Technion–Israel Institute of Technology, Haifa 32000, Israel*
[2]*Swiss Light Source, Paul Scherrer Institute, CH-5232 Villigen PSI, Switzerland*

(Received 25 August 2013; published 31 March 2014)

We report angle-resolved photoemission spectroscopy on two families of high-temperature superconductors $(\mathrm{Ca}_x\mathrm{La}_{1-x})(\mathrm{Ba}_{1.75-x}\,\mathrm{La}_{\,0.25+x})\mathrm{Cu}_3\mathrm{O}_y$ with $x = 0.1$ ($T_c^{\max} = 56$ K) and $x = 0.4$ ($T_c^{\max} = 82$ K). The Fermi surface (FS) is found to be independent of x or y, and its size indicates extreme sample-surface overdoping. This universal FS allows the comparison of dynamical properties between superconductors of similar structure and identical doping, but different $T_c^{\max}$. We find that the high-energy ($|E| > 50$ meV) nodal velocity in the $x = 0.4$ family is higher than in the $x = 0.1$ family. The implied correlation between $T_c^{\max}$ and the hopping rate t supports the notion of kinetic energy driven superconductivity in the cuprates. We also find that the antinodal gap is higher for the $x = 0.4$ family.

DOI: 10.1103/PhysRevB.89.121119 PACS number(s): 74.72.Gh, 74.25.Jb, 79.60.−i

The recent synthesis of charge compensated $(\mathrm{Ca}_x\mathrm{La}_{1-x})(\mathrm{Ba}_{1.75-x}\mathrm{La}_{0.25+x})\mathrm{Cu}_3\mathrm{O}_y$ (CLBLCO) single crystals, with $x = 0.1$ and $x = 0.4$, facilitates an investigation of the relationship between their dynamical properties, such as the electronic dispersion relation $E(\mathbf{k})$ and their thermodynamic property T_c, while applying subtle crystal structure changes [1]. Since the valence of Ca and Ba is equal, x has a minute effect on crystal structure but a large effect on T_c. Therefore, CLBLCO allows experiments where the correlations between T_c and a single parameter are explored. Experiments of such nature can reveal the mechanism for cuprates' superconductivity. In the present work, we measure the electron dispersion $E(\mathbf{k})$ of two extreme samples of CLBLCO crystals, using angle-resolved photoemission spectroscopy (ARPES), and look for correlations between properties of $E(\mathbf{k})$ and T_c. In particular, we focus on the nodal velocity. Previously, similar studies could only be done by comparing cuprates with very different structures and levels of disorder [2].

CLBLCO is similar to YBCO in crystal structure, but has no oxygen chain ordering and is tetragonal for all x and y [3]. This simplifies the ARPES interpretation. While x alters the calcium-to-barium ratio, the lanthanum content in the chemical formula remains constant. We define four CLBLCO "families" as samples with different x, namely, $x = 0.1, 0.2, 0.3, 0.4$. The parameter y signifies the oxygen level, which drives the system between different phases. By varying x and y in the chemical formula, one can generate phase diagrams that are similar in shape yet differ in the maximum of T_c, T_g, and T_N, and in the critical oxygen level at which the nature of the phase diagram changes. The phase diagram is presented in Fig. 1(a) [4]. It is worth noting that the only structural properties that vary with x or y are the Cu-O-Cu buckling angle, bond length, and CuO_2 plane doping efficiency $K(x)$. The crystallographic parameters were measured with powder neutron diffraction [5]. The buckling angle decreases by 0.5 degrees as x increases between families. The bond length varies from 3.88 Å for $x = 0.4$ to 3.91 Å at $x = 0.1$. The doping efficiency is determined by in-plane ^{17}O nuclear quadrupole resonance (NQR) [4]. The variation in the number of holes on an oxygen Δn_{p_σ} is given by $\Delta n_{p_\sigma} = K(x)(y - y_N)$, where y_N is defined as the doping at which T_N starts to drop [see Fig. 1(a)] [4].

The superexchange parameter J for each CLBLCO family was previously determined with muon spin rotation (μSR) (magnetization) versus temperature measurements [6] and with two-magnon Raman scattering [7]. Figure 1(b) depicts the superexchange J and glass temperature T_g (both from μSR), and T_c, all normalized by $T_c^{\max}$, as a function of Δn_{p_σ}. A universal phase diagram appears, demonstrating that $T_c^{\max}$ scales like J [4], which implies that $T_c^{\max}$ is determined by the overlap of the orbital occupied by electrons on neighboring sites. Orbital overlaps also determine the hopping parameter t, and the scaling of $T_c^{\max}$ with J meaning that kinetic energy controls the superconducting phase transition. However, J is determined in the AFM phase, which is "far," in terms of doping, from the superconducting phase. A question arises: are the orbital overlaps important in the superconducting phase as well? In this phase t can be measured directly. Here, we extract t from $E(\mathbf{k})$ as the velocity in the nodal direction. We find correlations between $T_c^{\max}$ and t, and confirm the famous relation $J \propto t^2$ [8]. This suggests that the band structure is rigid as a function of doping, as suggested by recent resonance inelastic x-ray scattering experiments [9]. By the same token, we also measure the antinodal gaps and compare them with Hamiltonian parameters.

The ARPES experiments were performed on the SIS beamline at the Swiss Light Source on CLBLCO single crystals. These unique crystals were grown using the traveling floating zone method. A detailed discussion about growth and characterization of these crystals is given in [1]. For this experiment, samples with $x = 0.1$ and $x = 0.4$ were used. The samples were mounted on a copper holder with silver glue to improve electrical conductivity. The Fermi level and resolution were determined from the polycrystalline copper sample holder. The samples were cleaved *in situ* using a glued-on pin at $T = 10$–20 K. Circularly polarized light with $h\nu = 50$ eV was used. The spectra were acquired with a VG Scienta R4000 electron analyzer. Despite a base pressure of 5×10^{-11} torr, the samples' surface lifetime was only a few hours and a high-intensity beam was required for quick

©2014 American Physical Society

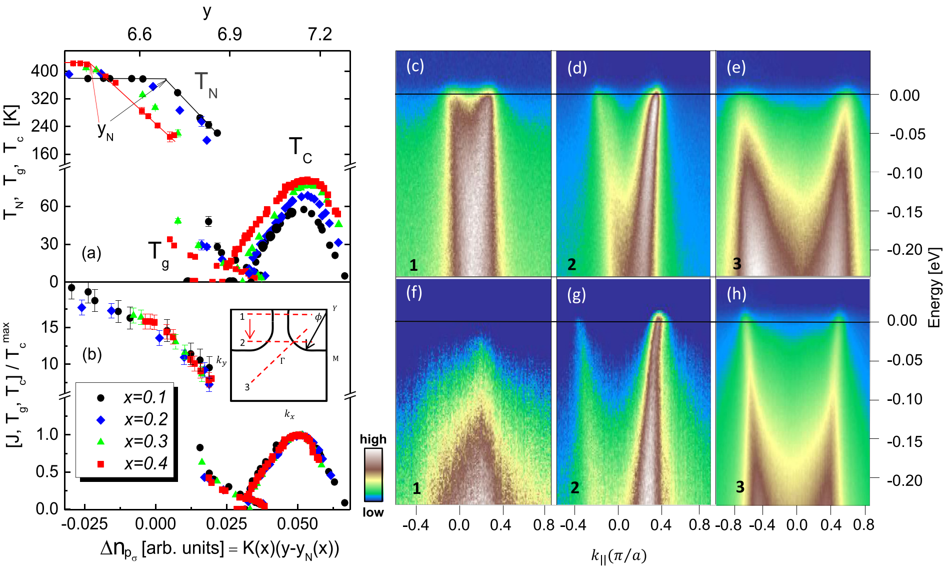

FIG. 1. (Color online) (a) The phase diagram of CLBLCO showing the Néel (T_N), glass (T_g), and superconducting (T_c) temperatures over the full doping range for the four families. y_N indicates the oxygen level where T_N start to drop. (b) The unified phase diagram of CLBLCO. The critical temperatures, and J extracted from T_N, are divided by $T_c^{\max}$ and plotted as a function of doping variation in the oxygen orbital Δn_{p_σ}. (c)–(e) Raw ARPES date measured on a CLBLCO $x = 0.1$ crystal at $T = 16$ K. The numbers on the figures correspond to cut trajectories illustrated in the inset of the phase diagram. (f)–(h) The same as (c)–(e) but for a sample with $x = 0.4$ measured at $T = 11$ K.

measurements. As a consequence, the energy resolution in our experimental conditions was limited to 17–22 meV.

In Fig. 1, we present ARPES data collected from CLBLCO for the two samples: $x = 0.1$ is presented in panels (c)–(e), while $x = 0.4$ is depicted in panels (f)–(h). The data were collected at $T = 16$ K and 11 K for $x = 0.1$ and 0.4, respectively. All spectra are normalized by the measured detector efficiency. For each sample, intensities along three cuts are shown. The cuts are illustrated and numbered on the Fermi surface (FS) drawing in the inset of Fig. 1(b). Cuts numbered 1 and 2 are along k_x (Γ-M direction). These cuts allow better sensitivity to the gap size at the antinode. Cut number 3 is along the diagonal line of the BZ (Γ-Y). In this configuration, a measurement of velocity in the nodal direction is possible. The number on the bottom of each ARPES panel indicates the cut from which data are collected.

In Figs. 1(c) and 1(f), spectra near the antinode are plotted. While $x = 0.1$ shows high-intensity spectra up to E_f where no gap is visible, the $x = 0.4$ sample shows a depletion of intensity close to E_f, indicating a gap in the spectra at the antinode. For the $x = 0.1$, the gap, if one exists, is smaller than the experimental resolution. In Figs. 1(d) and 1(g), we plot the intensity closer to the node. For both the $x = 0.1$ and 0.4 sample, we clearly see the spectra crossing E_f indicating a closed gap in the nodal region. Finally, in Figs. 1(e) and 1(h), both nodal cuts are seen, and again, the spectra cross E_f, indicating an absence of a gap along the Fermi arc for both samples. The last panels also show a clear dispersion from which the nodal velocity is extracted.

In Fig. 2, we show the FS in the first Brillouin zone (BZ), for the two CLBLCO samples: $x = 0.1$ [Fig. 2(a)] and 0.4 [Fig. 2(b)]. The FS was obtained by integrating 10 meV around the chemical potential. The ARPES intensity is displayed in a false-color scale as a function of k_x and k_y. By comparing the shape of the FS, we can see that the $x = 0.4$ sample exhibits a Fermi arc structure [10], which is typical for an antinodal gap. As for the $x = 0.1$ sample, the arc is not present, and we observed strong intensity at the antinode, comparable to the intensity near the nodal region. Unlike previously reported FS measurements of YBCO [11], there is no apparent chainlike structure in the CLBLCO FS, as expected. The red line is a fit to a tight binding (TB) model up to three nearest neighbors hopping. The fit parameters will be discussed below. The fit for both FSs gives the same size, as can be seen in Fig. 2. In fact, the FS of a variety of samples was measured and found to be identical regardless of family (x) or bulk oxygen level (y).

A clearer comparison of the FS size and doping between families can be obtained by examining the node-to-node and antinodal distances. In Fig. 2(c), we show momentum distribution curves (MDCs) at zero binding energy (E_f) measured in a nodal cut (“cut 3”), for both samples. The MDC for $x = 0.4$ is sharper than for $x = 0.1$, but the peak-to-peak distance is equal for both MDCs. Similarly, Fig. 2(d) depicts an MDC measured in the antinode (“cut 2”) at E_f. Here, the MDC of $x = 0.1$ is clearer than that of $x = 0.4$ because of an open gap, but again the peak separation for both samples is identical.

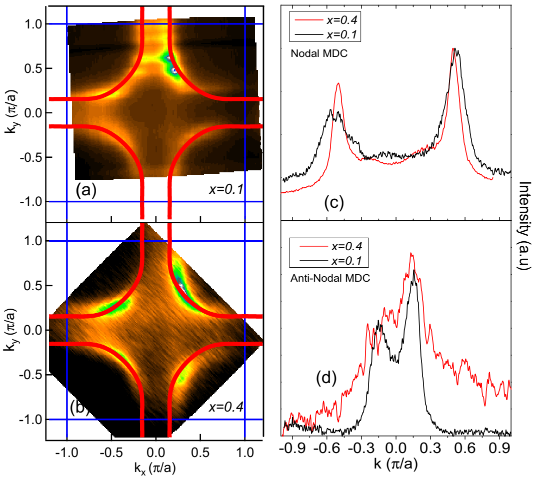

FIG. 2. (Color online) (a), (b) Spectral weight map in **k** space at E_f (FS) in CLBLCO $x = 0.1$ and $x = 0.4$ sample, respectively. The data were obtained at $T = 16$ K for the $x = 0.1$ sample and at $T = 11$ K for the $x = 0.4$ sample. Both samples were prepared with optimal doping and verified with a SQUID magnetometer. The red curve is the FS of CLBLCO obtained from tight binding fits to experimental data (see text). (c) MDCs at zero binding energy along a nodal cut, for the $x = 0.1$ [black, Fig. 1(e)] and $x = 0.4$ [red, Fig. 1(h)] samples. (d) MDCs at zero binding energy along the antinodal cut, for the $x = 0.1$ [black, Fig. 1(d)] and $x = 0.4$ [red, Fig. 1(g)] samples.

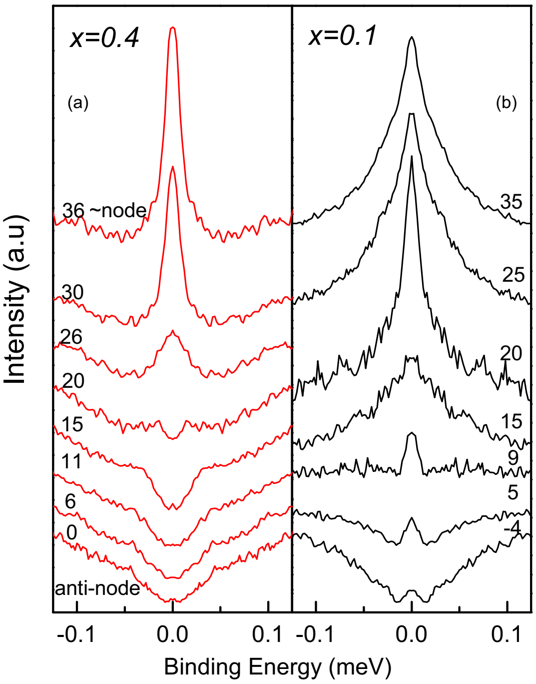

FIG. 3. (Color online) (a) Symmetrized EDCs for the $x = 0.4$ sample at k_f as a function of the Fermi surface angle ϕ, from the node (top) to the antinode (bottom). The cuts are measured along the Γ-M direction. Each curve is offset for clarity. (b) The same as (a) but for the $x = 0.1$ sample.

We suspect that the bulk doping independence of the FS is due to the sample being cleaved on a charged plane, inducing surface charge reconstruction. Such behavior was previously reported from measurements of YBCO [11]. From the measured nodal peak-to-peak distance as a function of doping in YBCO described in [11], we can estimate the doping of our sample, which turns out to be $p = 0.23 \pm 0.02$. This result is consistent with calculations based on the FS volume. Thus, we can conclude that the surface doping level of both samples is equal within the experimental error, and that the surface doping is on the edge of the superconducting dome on the overdoped side.

To investigate the momentum dependence of the gap, we measured the dispersion along Γ-M cuts between "cut 1" and "cut 2" for the $x = 0.1$ and $x = 0.4$ samples at a cold-finger temperature of $T = 16$ K and $T = 11$ K, respectively. In Fig. 3, we plot symmetrized EDCs at k_f as a function of FS angle ϕ (defined in the inset of Fig 1). For the $x = 0.4$ sample [Fig. 3(a)], one can see a zero-energy intensity peak close to the node ($\phi = 36$). In contrast, at an angle of $\phi = 20$ and lower, we observe an opening of a gap, which grows up to $\Delta_0 = 40$ meV at the antinode ($\phi = 0$). The angular dependence of the gap is shown in Fig. 1 of the Supplemental Material [12]. The gap value at the antinode is similar to optimally doped Bi2212 [13,14] and YBCO [15,16].

For the $x = 0.1$ sample [Fig. 3(b)], the situation is different. Close to the node, we observe a strong peak at zero energy ($\phi = 35$). As we move to the antinode, the intensity at zero energy is partly suppressed, but unlike the $x = 0.4$ sample, there is no full depletion of spectral density at $E = 0$. This indicates that a gap is not present in the $x = 0.1$ sample, or that it is smaller than the experimental resolution (20 meV). A closed gap was measured with the same resolution for two more $x = 0.1$ samples. Thus, we can safely say that $\Delta_0(x = 0.4) > \Delta_0(x = 0.1)$.

Last but not least, we compare the nodal velocity between families. This study was performed on six $x = 0.1$ and seven $x = 0.4$ crystals. The dispersion in the nodal direction, previously described in Figs. 1(e) and 1(h), was measured for each sample in two branches with high statistics. The samples were first oriented using a manipulator with six degrees of freedom in a procedure which is described in the Supplemental Material [17]. This lead to a k resolution of 0.005 (π/a) determined by our ability to find the node to node direction. The peak positions in the MDC of each measured dispersion was extracted and plotted as a function of binding energy. Exemplary dispersions of two samples are shown in Fig. 4. An axis breaker is used in order to show the two branches. The breaker emphasizes the differences between k_f of the two samples, which in fact is very small. Two different linear regimes are observed. The first regime involves low energies close to E_f, between $-50 < E < 0$ meV. The second regime corresponds to high energies where

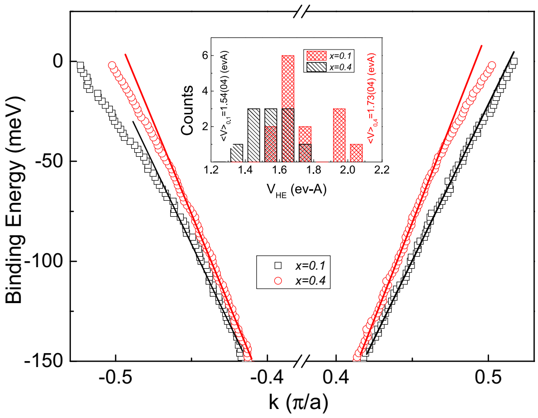

FIG. 4. (Color online) Main: The MDC peak position, extracted from the nodal dispersion measured along Γ-Y, as a function of k for $x = 0.1$ (black squares) and $x = 0.4$ (red circles). Note the axis breaker. The solid lines are a linear fit to the data in the $-150 < E < -50$ meV range from which the high-energy velocities V_{HE} are extracted. Inset: A histogram of high-energy velocities obtained from a series of CLBLCO samples with $x = 0.1$ (black, filled) and $x = 0.4$ (red, crossed).

$-150 < E < -50$ meV. The transition between these regimes is known as the kink and involves the electron dispersion renormalized due to correlations [18] or coupling between electrons and low-energy bosonic degrees of freedom [19]. The slope of the dispersion $\partial E/\partial k$ provides the velocity in the low- (v_F) and high-energy (v_{HE}) regimes. The results are similar to other overdoped materials [20].

We did not find differences with statistical significance in v_F between samples with different x. This is in agreement with previous work [20]. As for v_{HE}, the results are summarized in the inset of Fig. 4 as histograms. For the $x = 0.1$ family, the average high-energy velocity is $\langle V_{HE}^{0.1} \rangle = 1.53(04)$ eV Å, while for the $x = 0.4$ it is $\langle V_{HE}^{0.4} \rangle = 1.73(04)$ eV Å. Despite the velocity distribution overlap, the average velocities differ by 3.5σ, and hence are statistically different with 99.5% confidence. Using these velocities we can now calculate all the TB coefficients by $\partial E/\partial k = 4at\,\sin(k_f^{\text{node}} a)$. The unit cell parameter $a = 3.91$ Å is nearly family independent [5]. The coefficients are presented in the Supplemental Material [21] and are in agreement with previously published values [22,23].

From the data presented, we can draw several conclusions. First, we discuss the ratio of velocities $(\langle V_{HE}^{0.4} \rangle / \langle V_{HE}^{0.1} \rangle)^2 \simeq 1.26 \pm 0.08$. Despite the large error bar, this ratio is very close to that expected from the ratio of the superexchange J between families. This ratio is given by $J(0.4)/J(0.1) = T_c^{\max}(0.4)/T_c^{\max}(0.1) \simeq 1.4$ (see Fig. 1). Therefore, the $J \propto t^2$ relation is obeyed, and $T_c^{\max}$ depends on orbital overlaps even when the measurements are done in the doped phase.

However, ARPES measurements do not necessarily represent the bulk properties. For example, the buckling angle might change close to the surface. Nevertheless, if this happens in CLBLCO, it might affect both families equally. The fact that the ratio of J measured magnetically agrees with the ratio of t^2 measure by ARPES supports this notion.

Second, we discuss the gap. There are three possible scenarios that explain the difference in the gap size: (I) A scenario where disorder leads to broadening of the band structure features in $x = 0.1$ which hide the gap. However, high-resolution powder x-ray diffraction [24] and NMR experiments [25] indicate that $x = 0.1$ samples are more ordered than $x = 0.4$ ones. (II) A scenario where Δ opens only below T_c. It could be that in our experiment the surface of the $x = 0.4$ sample is below T_c, but the $x = 0.1$ surface, is not since its T_c is lower. In this case only the $x = 0.4$ sample will show a gap. The problem with this scenario is the observation of a Fermi arc in $x = 0.4$, which does not exist below T_c in any other cuprate. (III) A scenario where both samples are above T_c, but there is an intrinsic difference in their gap size. The problem here is again that in other materials there is no gap above T_c in extreme overdoped samples [26]. Further experiments are needed to clarify this point.

In conclusion, we present ARPES data from CLBLCO. We find that the surface doping is independent of the bulk doping or the Ca to Ba ratio. We also demonstrate that the gap can be measured in this system. The hopping parameter t is larger for $x = 0.4$ than for $x = 0.1$ in the overdoped sides. This suggests that $T_c^{\max}$ is correlated with electron-orbital overlaps on neighboring sites.

Note added in proof. Recent NMR measurements indicate that in CLBLCO there is a gap above T_c in extreme overdoped samples [27]. This suggests that there is an intrinsic difference in the anti-nodal gap size between the two families.

This research was supported by the Israeli Science Foundation (ISF) and the joint German-Israeli DIP Project.

---

[1] G. Drachuck *et al.*, J. Supercond. Novel Magn. **25**, 2331 (2012).
[2] B. Edegger, V. N. Muthukumar, C. Gros, and P. W. Anderson, Phys. Rev. Lett. **96**, 207002 (2006); E. Pavarini, I. Dasgupta, T. Saha-Dasgupta, O. Jepsen, and O. K. Andersen, *ibid.* **87**, 047003 (2001).
[3] A. Knizhnik, Y. Direktovich, G. M. Reisner, D. Goldschmidt, C. G. Kuper, and Y. Eckstein, Physica C **321**, 199 (1999).
[4] E. Amit and A. Keren, Phys. Rev. B **82**, 172509 (2010).
[5] R. Ofer, A. Keren, O. Chmaissem, and A. Amato, Phys. Rev. B **78**, 140508(R) (2008).
[6] R. Ofer, G. Bazalitsky, A. Kanigel, A. Keren, A. Auerbach, J. S. Lord, and A. Amato, Phys. Rev. B **74**, 220508(R) (2006).
[7] D. Wulferding, M. Shay, G. Drachuck, R. Ofer, G. Bazalitsky, Z. Salman, P. Lemmens, and A. Keren, arXiv:1402.7053.
[8] H. Eskes and R. Eder, Phys. Rev. B **54**, R14226 (1996).
[9] M. Le Tacon, G. Ghiringhelli, J. Chaloupka, M. Moretti Sala, V. Hinkov, M. W. Haverkort, M. Minola, M. Bakr, K. J. Zhou, S. Blanco-Canosa, C. Monney, Y. T. Song, G. L. Sun, C. T. Lin, G. M. De Luca, M. Salluzzo, G. Khaliullin, T. Schmitt, L. Braicovich, and B. Keimer, Nat. Phys. **7**, 725 (2011); M. P. M. Dean, G. Dellea, R. S. Springell,

F. Yakhou-Harris, K. Kummer, N. B. Brookes, X. Liu, Y.-J. Sun, J. Strle, T. Schmitt, L. Braicovich, G. Ghiringhelli, I. Boovi, and J. P. Hill, Nat. Mater. **12**, 1019 (2013).

[10] A. Kanigel, M. R. Norman, M. Randeria, U. Chatterjee, S. Souma, A. Kaminski, H. M. Fretwell, S. Rosenkranz, M. Shi, T. Sato, T. Takahashi, Z. Z. Li, H. Raffy, K. Kadowaki, D. Hinks, L. Ozyuzer, and J. C. Campuzano, Nat. Phys. **2**, 447 (2006).

[11] M. A. Hossain, J. D. F. Mottershead, D. Fournier, A. Bostwick, J. L. McChesney, E. Rotenberg, R. Liang, W. N. Hardy, G. A. Sawatzky, I. S. Elfimov, D. A. Bonn, and A. Damascelli, Nat. Phys. **4**, 527 (2008); D. Fournier, G. Levy, Y. Pennec, J. L. McChesney, A. Bostwick, E. Rotenberg, R. Liang, W. N. Hardy, D. A. Bonn, I. S. Elfimov, and A. Damascelli, *ibid.* **6**, 905 (2010).

[12] See Supplemental Material at http://link.aps.org/supplemental/10.1103/PhysRevB.89.121119 for description of the nodal velocity measurement procedure.

[13] U. Chatterjee, M. Shi, D. Ai, J. Zhao, A. Kanigel, S. Rosenkranz, H. Raffy, Z. Z. Li, K. Kadowaki, D. G. Hinks, Z. J. Xu, J. S. Wen, G. Gu, C. T. Lin, H. Claus, M. R. Norman, M. Randeria, and J. C. Campuzanoa, Nat. Phys. **6**, 99 (2010).

[14] J. Mesot, M. R. Norman, H. Ding, M. Randeria, J. C. Campuzano, A. Paramekanti, H. M. Fretwell, A. Kaminski, T. Takeuchi, T. Yokoya, T. Sato, T. Takahashi, T. Mochiku, and K. Kadowaki, Phys. Rev. Lett. **83**, 840 (1999).

[15] D. H. Lu, D. L. Feng, N. P. Armitage, K. M. Shen, A. Damascelli, C. Kim, F. Ronning, Z.-X. Shen, D. A. Bonn, R. Liang, W. N. Hardy, A. I. Rykov, and S. Tajima, Phys. Rev. Lett. **86**, 4370 (2001).

[16] Mike Sutherland, D. G. Hawthorn, R. W. Hill, F. Ronning, S. Wakimoto, H. Zhang, C. Proust, E. Boaknin, C. Lupien, M. A. Tanatar, J. Paglione, R. Liang, D. A. Bonn, W. N. Hardy, and Louis Taillefer, Physica C **408–410**, 672 (2004).

[17] See Supplemental Material at http://link.aps.org/supplemental/10.1103/PhysRevB.89.121119 for the gap angular dependence.

[18] T. Sato, H. Matsui, T. Takahashi, H. Ding, H.-B. Yang, S.-C. Wang, T. Fujii, T. Watanabe, A. Matsuda, T. Terashima, and K. Kadowaki, Phys. Rev. Lett. **91**, 157003 (2003).

[19] A. Lanzara, P. V. Bogdanov, X. J. Zhou, S. A. Kellar, D. L. Feng, E. D. Lu, T. Yoshida, H. Eisaki, A. Fujimori, K. Kishio, J.-I. Shimoyama, T. Noda, S. Uchida, Z. Hussain, and Z.-X. Shen, Nature (London) **412**, 510 (2001).

[20] X. J. Zhou, T. Yoshida, A. Lanzara, P. V. Bogdanov, S. A. Kellar, K. M. Shen, W. L. Yang, F. Ronning, T. Sasagawa, T. Kakeshita, T. Noda, H. Eisaki, S. Uchida, C. T. Lin, F. Zhou, J. W. Xiong, W. X. Ti, Z. X. Zhao, A. Fujimori, Z. Hussain, and Z.-X. Shen, Nature (London) **423**, 398 (2003).

[21] See Supplemental Material at http://link.aps.org/supplemental/10.1103/PhysRevB.89.121119 for tight binding coefficients of CLBLCO.

[22] R. S. Markiewicz, S. Sahrakorpi, M. Lindroos, H. Lin, and A. Bansil, Phys. Rev. B **72**, 054519 (2005).

[23] M. R. Norman, M. Randeria, H. Ding, and J. C. Campuzano, Phys. Rev. B **52**, 615 (1995),

[24] S. Agrestini, S. Sanna, K. Zheng, R. De Renzi, E. Pusceddu, G. Concas, N. L. Saini, and A. Bianconi, J. Phys. Chem. Solids **75**, 259 (2014).

[25] A. Keren, New J. Phys. **11**, 065006 (2009).

[26] U. Chatterjee, J. Zhao, D. Ai, S. Rosenkranz, A. Kaminski, H. Raffy, Z. Z. Li, K. Kadowaki, M. Randeria, M. R. Norman, and J. C. Campuzano, Proc. Natl. Acad. Sci. U.S.A. **108**, 9346 (2011).

[27] T. Cvitanic, D. Pelc, M. Pozek, E. Amit, and A. Keren, arXiv:1403.5574.

SUPPLEMENTARY MATERIAL FOR LINKING DYNAMIC AND THERMODYNAMIC PROPERTIES OF CUPRATES: AN ARPES STUDY OF $(\mathbf{CA}_x\mathbf{LA}_{1-x})(\mathbf{BA}_{1.75-x}\mathbf{LA}_{0.25+x})\mathbf{CU}_3\mathbf{O}_y$ (x=0.1 AND 0.4)

Gap Angular Dependence

In Figure 1 we plot the gap size as a function of Fermi surface angle for the $x = 0.4$ sample. The value of gap, extracted from the symmetrized EDC's shown in the article, is half of the peak-to-peak distance or the change in slope of the EDC.

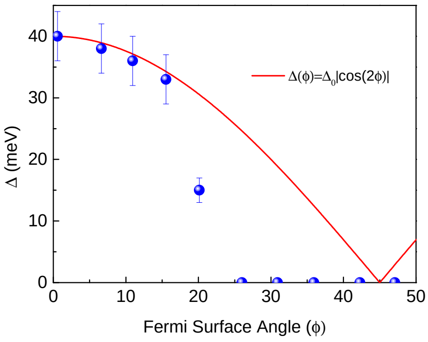

FIG. 1: Gap size as a function of Fermi surface angle ϕ for the $x = 0.4$ sample. The red line is the d-wave gap function, $\Delta(\phi) = \Delta_0|\cos(2\phi)|$, with $\Delta_0 = 40$ meV.

Nodal Cut Measurement

Because of the importance of proper orientation for the determination of the nodal velocity, we developed an alignment protocol. First, we map the complete FS of each sample in the first BZ. We define three angles, which can be manipulated, as shown in the inset of Fig. 2(a). $\theta = 0$, $\varphi = 45$, and $\psi = 0$ define a nodal cut. The red strait line represents the analyzer opening. Second, the angle θ is adjusted to give a symmetric spectrum. Third, we performed measurements with an intentional shifts $\Delta\psi$ and $\Delta\varphi$ angle to ensure truly perfect alignment. From each measurement we extracted the $k-$space distance $\Delta k(\Delta\psi, \Delta\varphi)$ between the two Fermi points. Figure 2(a) presents $\Delta k(\Delta\psi, 0)$ for ψ variations in steps of 0.5 a degrees. Figure 2(b) depicts $\Delta k(0, \Delta\varphi)$ for φ rotations again in steps of 0.5 degrees. Due to the geometry of the FS the nodal distance should be shortest when the alignment is perfect. Indeed, in both cases, the shortest distance was measured when $\Delta\psi = \Delta\varphi = 0$. We could determine the node to node distance with an accuracy of 0.25 degrees. Since this distance is ~ 1 (π/a) the resolution is is 0.005 (π/a). The same procedure was repeated for each and every measured sample.

Tight Binding Parameters

The tight binding parameters for CLBLCO extracted from the Fermi surface and nodal velocity are given in the table.

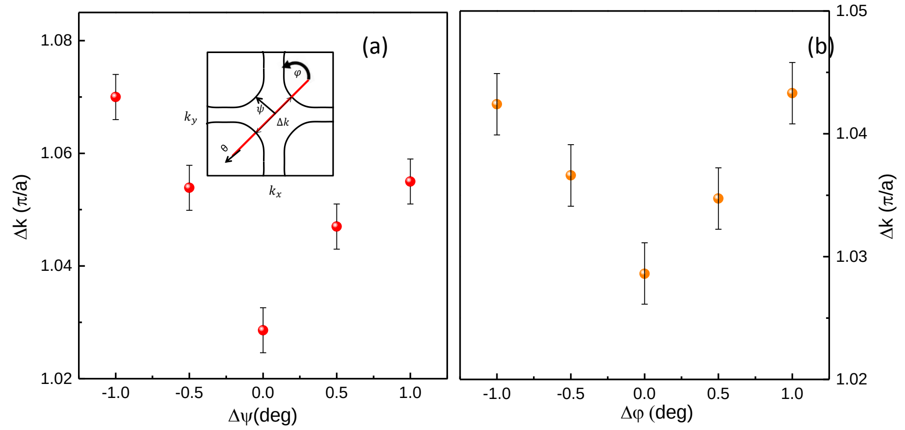

FIG. 2: (a) The nodal distance Δk as a function of the change in angle ψ, and (b) as a function of the change in angle φ. The inset shows an illustration of a nodal cut upon a FS, with the definition and action of θ, φ and ψ angles used in the experiment

i	$t_i^{x=0.1}$	$t_i^{x=0.4}$	$\eta_i(\mathbf{k})$
0	0.134	0.152	1
1	0.110	0.125	$-2\left[\cos\left(k_x a\right)+\cos\left(k_y a\right)\right]$
2	-0.032	-0.036	$-4\left[\cos\left(k_x a\right)\cos\left(k_y a\right)\right]$
3	0.016	0.018	$-2\left[\cos\left(2k_x a\right)+\cos\left(2k_y a\right)\right]$

TABLE I: Tight-binding coefficients and basis functions used to fit the experimental data. The second column lists the coefficient of each term in eV for the $x = 0.1$ and $x = 0.4$ samples, following the convention: $\varepsilon\left(\mathbf{k}\right) = \sum t_i \eta_i\left(\mathbf{k}\right)$

nature COMMUNICATIONS

ARTICLE

Received 6 Oct 2013 | Accepted 5 Feb 2014 | Published 27 Feb 2014

DOI: 10.1038/ncomms4390

Comprehensive study of the spin-charge interplay in antiferromagnetic $La_{2-x}Sr_xCuO_4$

Gil Drachuck[1], Elia Razzoli[2,3], Galina Bazalitski[1], Amit Kanigel[1], Christof Niedermayer[4], Ming Shi[2] & Amit Keren[1]

The origin of the pseudogap and its relationship with superconductivity in the cuprates remains vague. In particular, the interplay between the pseudogap and magnetism is mysterious. Here we investigate the newly discovered nodal gap in hole-doped cuprates using a combination of three experimental techniques applied to one, custom made, single crystal. The crystal is an antiferromagnetic $La_{2-x}Sr_xCuO_4$ with $x = 1.92\%$. We perform angle-resolved photoemission spectroscopy measurements as a function of temperature and find: quasi-particle peaks, Fermi surface, anti-nodal gap and below 45 K a nodal gap. Muon spin rotation measurements ensure that the sample is indeed antiferromagnetic and that the doping is close, but below, the spin-glass phase boundary. We also perform elastic neutron scattering measurements and determine the thermal evolution of the commensurate and incommensurate magnetic order, where we find that a nodal gap opens well below the commensurate ordering at 140 K, and close to the incommensurate spin density wave ordering temperature of 30 K.

---

[1] Department of Physics, Technion—Israel Institute of Technology, Haifa 32000, Israel. [2] Swiss Light Source, Paul Scherrer Institute, Villigen PSI CH-5232, Switzerland. [3] Departement de Physique and Fribourg Center for Nanomaterials, University de Fribourg, Fribourg CH-1700, Switzerland. [4] Laboratory for Neutron Scattering, Paul Scherrer Institute, Villigen PSI CH-5232, Switzerland. Correspondence and requests for materials should be addressed to G.D. (email: gil.drchk@gmail.com) or to A.K. (email: keren@physics.technion.ac.il).

© 2014 Macmillan Publishers Limited. All rights reserved.

Recent low-temperature angle-resolved photoemission spectroscopy (ARPES) experiments on the underdoped cuprate superconductors indicate the presence of a fully gapped Fermi surface (FS)[1–4]; even in the antiferromagnetic phase[5]. The natural candidates for opening such a gap are charge or spin density waves (SDW). Out of all hole-doped cuprates, $La_{2-x}Sr_xCuO_4$ (LSCO) is the most promising material for exploring whether a SDW is indeed responsible for this gap. LSCO single crystals with large size allow for magnetic measurements such as muon spin rotation (μSR) and neutron diffraction (ND), simultaneously with ARPES. The magnetic probes can characterize the SDW while ARPES explores the gap.

However, the region of the phase diagram where the magnetic properties are clearly exposed is different from the region where the band dispersion is visible. On the one hand, long-range magnetic order disappears as doping approaches 2% from below, hindering our ability to perform ND. On the other hand, LSCO becomes insulating at low temperature as the doping approaches 2% from above, thus restricting ARPES. In fact, ARPES data for LSCO with doping lower than 3% are rare and missing the quasiparticle peaks in the energy distribution curves (EDCs)[2,6]. The main problem is the high resistivity of extremely underdoped samples, which is detrimental to ARPES due to charging effects. Nevertheless, the resistivity of LSCO as a function of temperature, at 2% doping, has a broad minimum around 100 K[7]. This minimum insures that resistivity is finite even at lower temperatures and opens a window for both experiments.

By preparing a series of LSCO single crystals with ~0.2–0.3% doping steps around 2%, we manage to find one to which all techniques apply. This allows us to explore the cross-talk between the magnetic and electronic properties of the material. We find that the charge excitation are impartial to the commensurate spin order. However, the nodal gap opens at a temperature very close to the one where an incommensurate SDW sets in. The small temperature mismatch is assigned to experimental sensitivity.

Results

The magnetic order. The series of samples are first characterized by μSR. In Fig. 1, we show the μSR frequency as a function of temperature for all crystals. In samples with doping equal to or less than 2%, the oscillation starts at temperatures on the order of 100 K. At 2%, there is a sharp transition from the antiferromagnetic long-range order to the spin-glass state where the same oscillations appear only at temperatures on the order of 10 K (refs 8,9). More details of the μSR characterization of the samples are given below and in the Methods section. We perform the ND and ARPES measurements on a sample with $x = 1.92\%$ (red rhombuses) that is antiferromagnetic with a Néel temperature $T_N \simeq 140$ K.

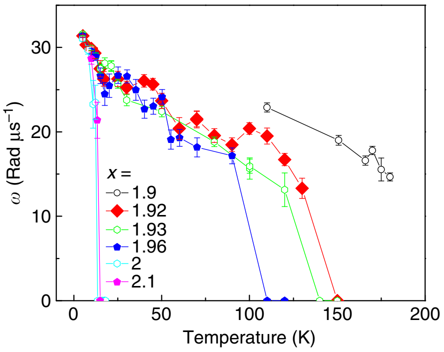

Figure 1 | μSR frequency as a function of temperature. μSR frequency as a function of temperature for LSCO single crystals with different x values. At $x = 2\%$, there is a clear transition from an antiferromagnetic to a spin-glass ground states. The data in the rest of this paper are measured on the $x = 1.92\%$ sample, which is in the antiferromangetic phase. The error bars were determined from the data fitting procedure described in the Methods section.

The FS. Figure 2a shows the ARPES intensity map near the Fermi level (E_F) in the second Brillouin zone, measured along cuts parallel to cut 1 and 2 shown in the figure. The high intensities represent the underlying FS and has the morphology of the FS in more doped LSCO[10] and other cuprates. Most of the intensity is centred around the zone diagonal on the $(0, -2\pi/a)$ to $(\pi/a, -\pi/a)$ line. This suggests the presence of gapped electronic excitations in the off-diagonal $(0, -\pi/a)$ region. Similar results were obtained at a higher doping level of $x = 3-8\%$ (ref. 4).

The magnetic structure. Figure 2b depicts ND for the same sample at 3 K. The scans are performed along the red line, in a

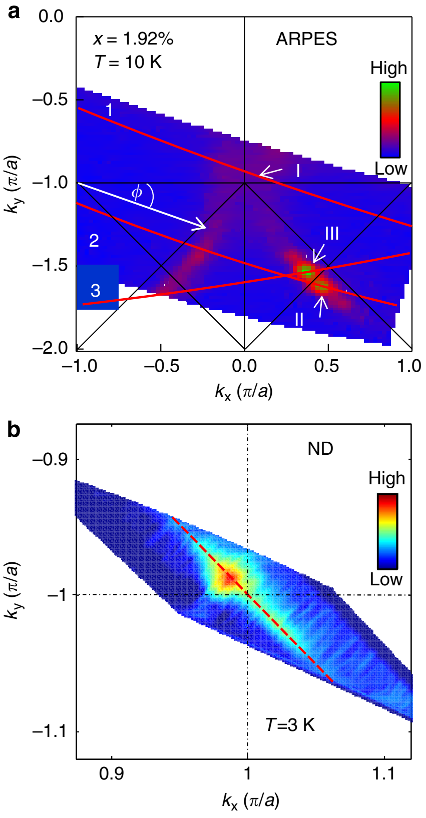

Figure 2 | The Fermi surface and incommensurate magnetic order in LSCO with 1.92% doping. (**a**) Low-energy ARPES data in the second Brillouin zone. The red lines 1 and 2 show cuts on which data were collected. Line 3 is the cut on which temperature dependence data are presented in Fig. 3. Point I, II and III mark points where EDCs are extracted. The intensity is centred in the diagonal region. (**b**) ND measurements at 3 K in a small region around a magnetic reciprocal lattice vector showing a strong and feeble incommensurate peaks. The dashed red line depicts the measurements scan direction.

© 2014 Macmillan Publishers Limited. All rights reserved.

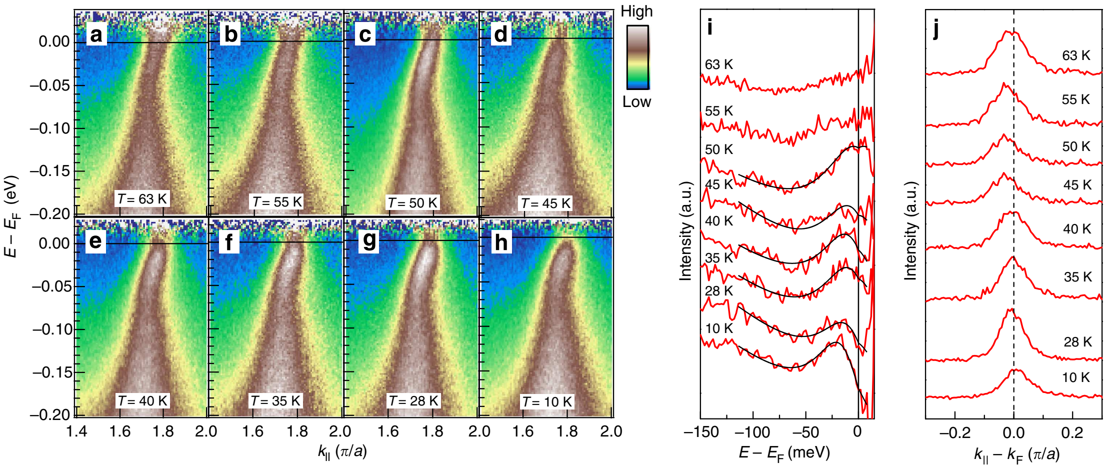

Figure 3 | Temperature dependent ARPES data. (**a**–**h**) ARPES spectra along a cut given by line 3 in Fig. 1. The spectra are divided by resolution broadened Fermi-Dirac distribution. At high *T*, the spectrum crosses the Fermi energy. At low *T*, it does not. (**i**) EDCs at the Fermi momentum of point III in Fig. 1b for different temperatures. The solid lines are guides to the eye. At 10 K, the peak is clearly below the Fermi energy. $\Delta(T)$ is presented in Fig. 4c. (**j**) MDC at E_F as a function of temperature showing that k_F in the diagonal region is temperature independent.

narrow range in the reciprocal lattice space centred around the (1, − 1) point, in the standard tetragonal ARPES units of π/a. In fact, the scanned area of the ND experiment in k-space is only a small fraction of the scanned area of the ARPES. A clear breaking of the fourfold symmetry is observed in this figure. In addition, two incommensurate peaks are present in the centre of the figure: one is clearly observed as a red spot, and the other is weak and will be demonstrated below. Such incommensurate peaks occur when, on top of the main magnetic order, the system develops spin modulations (stripes) running in diagonal to the bond directions (diagonal stripes). The stripes and commensurate scattering observed in our sample are in agreement with previous reports for low-doping LSCO[11,12], and are discussed further below.

The gap. In Fig. 3a–h, we show the temperature dependence of ARPES data in the vicinity of point III along cut 3 in Fig. 2a. All spectra are divided by resolution broadened Fermi-Dirac distribution at the nominal temperature. Data analysis by the Lucy–Richardson deconvolution method[13] is discussed in the Methods section. At high temperatures ($T > 50$ K), the dispersive peak crosses E_F as clearly seen in Fig. 3a. In contrast, at low temperatures ($T < 45$ K), there is a gap in the electronic spectra, that is, the peak position at k_F remains below E_F. A similar gap exists in LSCO up to 8% doping[4], in LBCO at 4% (ref. 2), in the electron doped compound[1], in Bi2212 (ref. 3) and La-Bi2201 (ref. 5). It also exsists in simulations where inhomogeneous SDW and superconductivity coexist[14] or Coulomb disorder effects are present[15]. EDCs extracted from Fig. 3a–h, at k_F given by point III of Fig. 2a, are plotted in Fig. 3i. The solid lines are guides to the eye. At temperatures above 45 K, the peak is at E_F. However, below this temperature the peaks are clearly below E_F, indicating the presence of a gap.

An important aspect of these EDCs is the fact that at all low temperatures, E_F is not in the middle of the gap, namely, the intensity of the spectra immediately above E_F is lower than at E_F. This could be an analysis artifact due to division by the resolution broadened Fermi-Dirac function[13] or indicate that the particle-hole symmetry is broken. Particle-hole asymmetry towards the diagonal region in the non-superconducting phase[16], and in the off-diagonal region[17], was found previously. However, it is very difficult to distinguish between the two options in our sample with extremely low carrier concentration.

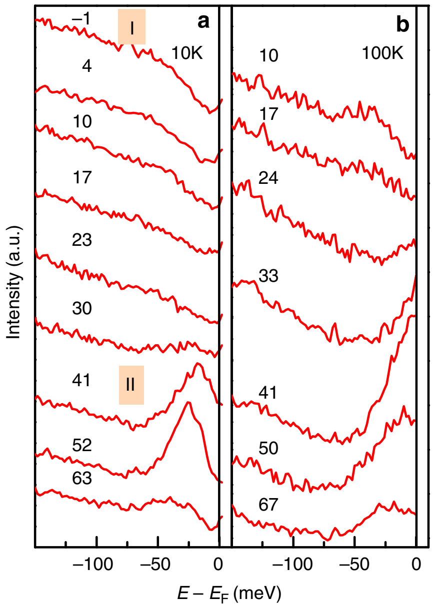

Figure 4 | Angular-dependent ARPES data. (**a**) EDCs at different k_F along the FS in two different temperatures. The Fermi surface angle ϕ is indicated above each EDC. Spectra I and II are taken at the k of point I and II in Fig. 1b that are defined by the crossing point between the red lines 1 and 2 and the FS. The other EDCs are from the crossing points in between. At 10 K, a gap is observed all around the FS. $\Delta(\phi)$ is presented in the inset of Fig. 5c. (**b**) Similar EDCs at 100 K. In this case, a gap is observed only in the off-diagonal region.

© 2014 Macmillan Publishers Limited. All rights reserved.

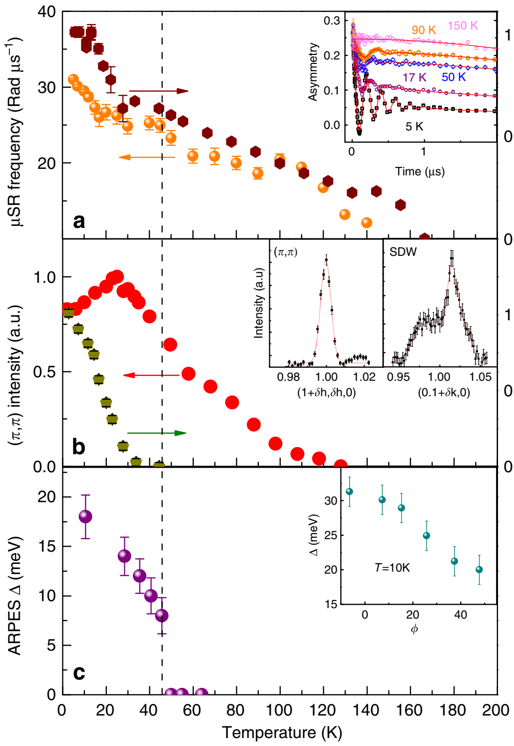

Figure 5 | Experimental parameters from all three techniques. (**a**) Muon rotation frequency and the magnetic volume fraction of the sample as a function of temperature taken from a fit to a three Lorentzian model (see Methods section). The inset shows raw data and the fit quality for the $x = 1.92\%$ sample. (**b**) Commensurate and incommensurate ND intensity. The SDW inset is the intensity versus k along the neutron scattering cut in Fig. 2c showing the strong and feeble incommensurate peaks. The (π, π) inset shows the commensurate peak. (**c**) ARPES nodal gap Δ at k_F, as obtained from the peaks in Fig. 3i, versus temperature. The inset shows the angular dependence of the gap $\Delta(\phi)$. The error bars were determined from the experimental resolution.

Another parameter relevant for understanding the mechanism by which the nodal gap opens is the temperature dependence of k_F. This is explored by extracting the momentum dispersion curve at E_F from Fig. 3a–h, as presented in Fig. 3j. The peak position fluctuates somewhat around a constant value as the temperature is lowered, indicating that $k_\mathrm{F} = 0.63(\pi/a)$ along the diagonal is temperature independent. Therefore, the high-intensity curves in Fig. 2b represents the FS.

The evolution of the gap around the FS is shown in Fig. 4a,b for 10 and 100 K. The spectra marked I and II in Fig. 4a are EDCs at the k_F of points I and II in Fig. 2a. The spectra in between correspond to k_F between points I and II. EDCs shown in Fig. 4b are from similar point along the FS. In the off-diagonal region, there is no spectral weight at E_F for both temperatures, indicating that the anti-nodal gap opens at a temperature higher than 100 K. In the diagonal region, there is high spectral weight at 100 K, but not at 10 K. Thus at 100 K, we observe a Fermi arc[18], while at 10 K, a gap appears all around the FS.

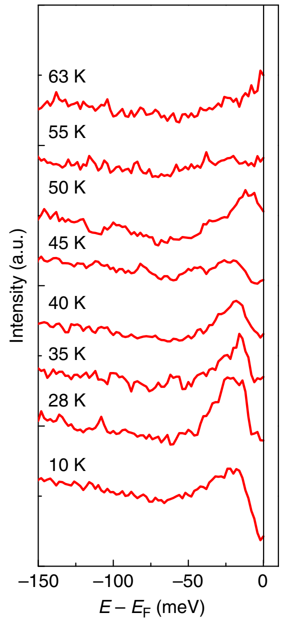

Figure 6 | The Lucy-Richardson method. The same data as in Fig. 3i but analysed using the Lucy-Richardson deconvolution method[13].

Summary of parameters. Finally, in Fig. 5, we present a summary of parameters extracted from all three techniques. Figure 5a shows the temperature dependence of the muon rotation frequency and magnetic volume fraction. The inset represents a fit of a three-component model, with one frequency, to the µSR data at different temperatures. More details are available in the methods section. The magnetic parameters grow upon cooling, saturate between 50 and 25 K, and grow again at lower temperatures. The temperature $T_\mathrm{F} = 25$ K was associated with hole freezing into one dimensional domain walls[8,9,19]. The restriction of the charge motion below T_F must be intimately related to the opening of the nodal gap.

Figure 5b shows the commensurate and the incommensurate scattering intensity. The insets show two raw data sets. The first is a scan along $(0,1+\delta k,0)$ (in orthorhombic units), which is the red diagonal line in Fig. 2b. This scan is sensitive to the incommensurate fluctuations and show two asymmetric peaks. The second scan is along $(1+\delta h,1,0)$ and detects only the commensurate order as a single peak. As the temperature is raised, the incommensurate intensity decreases until it disappears at $T_\mathrm{F} = 30$ K. The commensurate intensity peaks at 25 *K*, just when the muon oscillation changes its behaviour, and vanishes at $T_\mathrm{N} = 130$ K. Our ND temperature dependence results, shape of the peaks and incommensurability parameter (in tetragonal units) $\delta = 0.027(\pi/a)$ are in good agreement with previously reported data[12]. While the ND data are well understood in terms of a spiral ground state[20], its relation to the gap is still mysterious, since the nesting condition $k_F + \delta = \frac{\sqrt{2}\pi}{2a}$ is not fulfilled in our sample.

The nodal gaps at k_F, Δ, are determined from the peak in the EDCs of Fig. 3i and presented in Fig. 5c as a function of temperature. Very similar gap values are found using the Lucy–Richardson deconvolution method, shown in Fig. 6 (ref. 13). The gap opens at 45 K. The major observations in this figure are: (I) the nodal gap opens when the commensurate moment is about half its full value. (II) With temperature decreasing, the nodal gap first opens when the incommensurate moment is barely or not detectable.

© 2014 Macmillan Publishers Limited. All rights reserved.

The temperature mismatch between the opening of the nodal gap and appearance of the incommensurate peaks could be real, but most likely is an artifact. We determined the ARPES gap from the quasi-particle peaks. An alternative is to use the leading edge as the measure of the gap. The leading edge crosses the Fermi energy at a lower temperature than the peak. Therefore, the leading edge criteria would make the temperature mismatch smaller. In addition, the ND require both periodic and frozen magnetic moments on a time scale determined by the instrument resolution. ARPES is sensitive to shorter time scales than ND. Hence, lower temperature are required for ND to pick up the incommensurate signal than for ARPES to detect the gap. This experimental time scale difference between techniques is an alternative explanation to the temperature mismatch.

The angular dependence of the gaps is presented in the inset of Fig. 5c; the angle ϕ is defined in Fig. 2a. When a peak is absent, the gap is taken from the change of slope in the EDCs. $\Delta(\phi)$ is in agreement with previous measurements for 3–8% dopings[4].

Discussion

On the basis of weak coupling theory, Berg *et al.*[21] argued that the commensurate part of the SDW can open a nodal gap only if the moment is larger than a critical value. However, the opening of the gap will be accompanied by a shift in k_F. The effect of the incommensurate part of the SDW depends on the properties of time reversal followed by translation symmetry, which can be broken or unbroken. In the unbroken case, a nodal gap will open when the perturbation exceeds a critical value. Both these options do not agree with our data. In the broken symmetry case, a nodal gap can open for arbitrarily small perturbation with no impact on k_F. This option is in agreement with our measurements and bares important information on the symmetries of the ground state. Another possibility is that the gap is of the superconducting type, which maintains particle-hole symmetry and keeps k_F fixed. This option would mean that the cuprates have a superconducting gap in the antiferromagnetic phase.

In conclusion, we detect a nodal gap in the antiferromagnetic phase of LSCO. The gap opens well below T_N and very close to the temperature where incommensurate SDW is detected. This finding puts strong restrictions on the origin of the nodal gap.

Methods

μSR. The experiment was carried out at PSI on the GPS beam line. We fit the muon polarization as a function of time to

$$P_z(t) = (1-V_m)e^{-\frac{1}{2}D^2t^2} + V_m\left[p\times e^{-(R_1 t)^{b_1}} + (1-p)\times e^{-(R_2 t)^{b_2}}\cos(\omega t+\phi)\right] + P_{Bg} \qquad (1)$$

where ω is the muon rotation angular frequency, V_m stands for the magnetic volume fraction, p is the amplitude of the rotating signal resulting from the angle between the muon spin and the internal field, D, R_1 and R_2 are relaxation rates, b_1 and b_2 are stretching exponents, and P_{Bg} is the background polarization from muon that missed the sample. We could fit the data well with $b_1 = 0.5$ and $b_2 = 1$ for most of the temperatures. Between $T = 25$ to 50 K, we allowed freedom in their values to achieve an optimal fit.

ARPES. The experiment was done at the Swiss Light Source in PSI. The samples were mounted on a specialized holder, as described in Mansson *et al.*[22], with silver glue to improve electrical conductivity. The Fermi level and resolution were determined from the polycrystalline copper sample holder. The samples were cleaved *in situ* at $T = 10$ K under a ultrahigh vacuum better than 6×10^{-11} Torr. Circularly polarized light with $h\nu = 55$ eV was used. The spectra were acquired with a VG Scienta R4000 electron analyser. Charging tests have been carried out by varying the photon flux. No charging was found. In addition, after performing the high temperature measurements, the sample was cooled again and the results at 10 K were reproducible. We examined the surface with LEED at each temperature and no surface degeneration or reconstruction was found during the measurements.

It should be pointed out that in ARPES, the incoming light warms the surface, and there could be a few degrees difference between the sample surface temperature and the temperature of the cold finger which we quote in the paper.

EDCs obtained by Lucy–Richardson deconvolution method are depicted in Fig. 6.

Neutron diffraction. The ND experiments was carried out at Paul Scherrer Institute (SINQ, PSI) on the RITA-II beam line. The crystal was mounted on an aluminium sample holder with the crystallographic $\hat{\mathbf{c}}$-axis perpendicular to the neutron beam; that is, (1,0,0)–(0,1,0) scattering plane. The beam collimation was set to 80′-40′-80′. A beryllium filter was placed before the analyser to remove higher order neutrons. The instrument consisted of a nine-blade pyrolytic graphite analysers. The diffraction studies were performed with 4.04 Å (5 meV) neutrons, using all the blades in order to create a 2D intensity plot. The sample was aligned in such a manner that the area of interest (commensurate and incommensurate magnetism) was measured in the centre blade. The incommensurate part was measured in a $(0,1+\delta q,0)$ scan to avoid the commensurate contribution. The high temperature data weres subtracted to remove the leftover $\lambda/2$ contribution form the (0,2,0) structural Bragg peak. For the commensurate part, the measurement was performed with a scan direction $(1+\delta q,\delta q,0)$ to avoid the incommensurate contribution.

References

1. Harter, J. W. *et al.* Nodeless superconducting phase arising from a strong (π, π) antiferromagnetic phase in the infinite-layer electron-doped $La_{2-x}Sr_xCuO_4$ compound. *Phys. Rev. Lett.* **109,** 267001 (2012).
2. Valla, T. Angle-resolved photoemission from cuprates with static stripes. *Physica C* **481,** 66–74 (2012).
3. Vishik, I. M. *et al.* Phase competition in trisected superconducting dome. *Proc. Natl Acad. Sci. USA* **109,** 18332–18337 (2012).
4. Razzoli, E. *et al.* Evolution from a nodeless gap to $d_{x^2-y^2}$-wave in underdoped $La_{2-x}Sr_xCuO_4$. *Phys. Rev. Lett.* **110,** 047004 (2013).
5. Peng, Y. *et al.* Disappearance of nodal gap across the insulator superconductor transition in a copper-oxide superconductor. *Nat. Commun.* **4,** 2459 (2013).
6. Shen, K. M. *et al.* Fully gapped single-particle excitations in lightly doped cuprates. *Phys. Rev. B* **69,** 054503 (2004).
7. Ando, Y. *et al.* Electronic phase diagram of high-T_c cuprate superconductors from a mapping of the in-plane resistivity curvature. *Phys. Rev. Lett.* **93,** 267001 (2004).
8. Niedermayer, Ch. *et al.* Common phase diagram for antiferromagnetism in $Y_{1-x}Ca_xBa_2Cu_3O_6$ and $La_{2-x}Sr_xCuO_4$ as seen by muon spin rotation. *Phys. Rev. Lett.* **80,** 3843–3846 (1998).
9. Chou, F. C. *et al.* Magnetic phase diagram of lightly doped $La_{2-x}Sr_xCuO_4$ from ^{139}La nuclear quadrupole resonance. *Phys. Rev. Lett.* **71,** 2323–2326 (1993).
10. Razzoli, E. *et al.* The Fermi surface and band folding in $La_{2-x}Sr_xCuO_4$ probed by angle-resolved photoemission. *New J. Phys.* **12,** 125003 (2010).
11. Fujita, M. *et al.* Static magnetic correlations near the insulating-superconducting phase boundary in $La_{2-x}Sr_xCuO_4$. *Phys. Rev. B* **65,** 064505 (2002).
12. Matsuda, M. *et al.* Electronic phase separation in lightly doped $La_{2-x}Sr_xCuO_4$. *Phys. Rev. B* **65,** 134515 (2002).
13. Rameau, J. *et al.* Application of the Lucy-Richardson deconvolution procedure to high resolution photoemission spectra. *Electron. Spectrosc. Relat. Phenom.* **181,** 35–43 (2010).
14. Atkinson, W. A. *et al.* Robust nodal d-wave spectrum in simulations of a strongly fluctuating competing order in underdoped cuprate superconductors. *Phys. Rev. Lett.* **109,** 267004 (2012).
15. Chen, W. *et al.* Coulomb disorder effects on angle-resolved photoemission and nuclear quadrupole resonance spectra in cuprates. *Phys. Rev. B* **80,** 094519 (2009).
16. Yang, H.-B. *et al.* Emergence of preformed Cooper pairs from the doped Mott insulating state in $Bi_2Sr_2CaCu_2O_{8+}$. *Nature* **456,** 77–80 (2008).
17. Hashimoto, M. *et al.* Particle hole symmetry breaking in the pseudogap state of Bi2201. *Nat. Phys.* **6,** 414–418 (2010).
18. Kanigel, A. *et al.* Evolution of the pseudogap from Fermi arcs to the nodal liquid. *Nat. Phys.* **2,** 447–451 (2006).
19. Gooding, R. J. *et al.* Staggered magnetization in $La_{2-x}Sr_xCuO_4$ from ^{139}La NQR and μSR: effects of Sr doping in the range $0<x<0.02$. *Phys. Rev. B* **52,** 7334–7345 (1995).
20. Lüscher, A. *et al.* Structure of the spin-glass state of $La_{2-x}Sr_xCuO_4$: the spiral theory. *Phys. Rev. Lett.* **98,** 037001 (2007).
21. Berg, E. *et al.* Stability of nodal quasiparticles in superconductors with coexisting orders. *Phys. Rev. Lett.* **100,** 027003 (2008).
22. Mansson, M. *et al.* On-board sample cleaver. *Rev. Sci. Instrum.* **78,** 076103 (2007).

Acknowledgements

The Technion team was supported by the Israeli Science Foundation (ISF) and the joint German-Israeli DIP project. E.R. was partially supported by the Fonds National Suisse

© 2014 Macmillan Publishers Limited. All rights reserved.

pour la Recherche Scientifique through Div. II and the Swiss National Center of Competence in Research MaNEP. We thank the SLS, SμS and SINQ beam line staff at the Paul Scherrer Institute for their excellent support.

Author contributions

A.Ke. proposed and designed the research. G.D. and G.B. prepared and characterized the samples. G.D., E.R., A.Ke., A.Ka., C.N. and M.S. carried out and the experiment and data analysis. G.D. and A.Ke. wrote the paper.

Additional information

Competing financial interests: The authors declare no competing financial interests.

Reprints and permission information is available online at http://npg.nature.com/reprintsandpermissions/

How to cite this article: Drachuck, G. *et al.* Comprehensive study of the spin-charge interplay in antiferromagnetic $La_{2-x}Sr_xCuO_4$. *Nat. Commun.* 5:3390 doi: 10.1038/ncomms4390 (2014).

© 2014 Macmillan Publishers Limited. All rights reserved.

Chapter 4

Discussion

New Perspectives for Cuprate Research: CLBLCO Single Crystals

The successful growth of CLBLCO single crystals has opened new possibilities for experiments which previously were inaccessible for powder samples. However, a systematic study was needed to confirm that the new crystals have the same physical properties, in terms of the chemical composition, magnetic structure and superconductivity, as the old generation of CLBLCO samples. Furthermore, the quality of bulk and surface of the crystals had to be checked, in order to ensure their compatibility for advanced experimental techniques, such as ARPES, neutrons scattering and Raman spectroscopy.

The bulk characterization of the crystal was performed by a multitude of techniques. The bulk superconducting properties of this crystal were tested by transport and magnetization measurements. Crystals from the extreme families, $x = 0.1$ and 0.4, were annealed in oxygen to achieve optimal doping. Figure 3 shows normalized resistivity and susceptibility of both samples. At optimal doping T_c measured by resistivity for both families was found to be in perfect agreement with powder sample measurements. The superconducting volume fraction extracted from the magnetization measurement was approximately 100%. Inductively-coupled plasma atomic- emission spectroscopy

---

[1] The figure references in this chapter refer to the published papers

(ICP-AES) measurement revealed there is no difference in the Ca, Ba, or La content, between the crystals and powders [29].

The $x = 0.1$ samples were latter annealed in Argon atmosphere to remove oxygen in order to explore their magnetic properties with ZF-μSR. Figure 5 shows the moun polarization as well as the muon frequency at different temperatures. The sample was found to be AFM with T_N which is consistent with the well established phase diagram. A large $x = 0.1$ crystal (shown in Fig.2) were employed in neutron diffraction measurements. We detected the (100), (200), (110), (220) nuclear Bragg peaks as presented in Fig.4. The nuclear (001) and the magnetic ($\frac{1}{2}\frac{1}{2}1$) Bragg peaks were also detected. Unfortunately, latter neutron scattering experiment, intended to measure the spin-wave dispersion of CLBLCO were unsuccessful, despite the promising preliminary elastic and inelastic neutron scattering experiment. This is due to the low spin of cuprates which ($S = \frac{1}{2}$) which reduces the neutron scattering intensity. A Larger crystal mass is required for these experiments.

The quality of the crystal surface upon cleaving has been also explored. One sample was cleave and placed under a scanning electron microscope (SEM) equipped with a electron back-scatter diffraction module (EBSD) which provides a local crystal structure measurement[30]. Clear Kikuchi lines were measured from a flat crystal facet (Fig.6). The diffraction patterns revealed that the surface of the facet is perpendicular to the crystal c-axis, a geometry well suited to for studying the physics of the CuO_2 planes). Raman scattering experiment performed on CLBLCO confirmed the structure of the cleaved surface. Raman measurement also revealed optical phonon spectra of CLBLCO and two-magnon peak (Fig.7), paving the way for a more comprehensive Raman study of CLBLCO [20].

Linking dynamic and thermodynamic properties of cuprates: An angle-resolved photoemission study of CLBLCO

With the success of synthesizing single crystal of the extreme case families, ARPES experiments became applicable for the first time for CLBLCO. In the present work we measured the electron dispersion $E(\mathbf{k})$ of two extreme samples of CLBLCO crystals in search of correlation between the properties of the electronic dispersion and T$_c$. The universal phase diagram of CLBLCO demonstrated that T_c^{max} scales like J, the AFM super-exchange, which implies that T_c^{max} is in fact related to the kinetic energy t via the famous relation $J \propto t^2$ [31]. t was extracted from the Fermi velocity (v_F) in nodal direction.

In the ARPES experiment the Fermi surface of the CBLCO family was explored for the first time. In Fig.2 in the article, the FS of $x = 0.1$ and $x = 0.4$ crystal are presented. Initially, the motivation was to measure the doping evolution of the FS morphology. However as previously reported in YBCO, the [32, 33], CLBLCO cleaves on a non-neutral plane and the surface undergoes a charge reconstruction which fixes the doping to $p = 0.23 \pm 0.02$ holes per unit cell, regardless of the initial doping of the sample. The two FS presented in the article were fitted with the same tight binding (TB) model from which the number oh hole were extracted using Luttinger's sum rule. The TB coefficient are given in the supplemental material for the article and are in agreement with previously reported values [34].The resulting doping, which was confirmed by measuring the node to node distance and comparing it to previously publish data from YBCO [33]. It is worth noting that, in contrast to YBCO, there is no apparent chainlike structure in the FS of CLBLCO, in agreement with previously reported data on CLBLCO [17].

The magnitude of the gap, as well as its momentum dependence has been measured for CLBLCO with $x = 0.1$ and 0.4. The electronic dispersion was measured along Γ-M cuts form the anti-node through the node. Symmetrized EDC's at k_F as a function of the FS angle, are shown in Fig.3 of the article. For the $x = 0.4$ sample, zero-energy intensity peaks were measured close to the node. In contrast, approaching the anti-node, an opening of the gap has been observed, with a magnitude of $\Delta_0 = 40$ meV. For the

$x = 0.1$ sample, strong peaks at zero energy were measured close to the node, but no full depletion of spectral density was detected at the anti-node. This indicates that a gap is not present in the x = 0.1 sample, or that it is smaller than the experimental resolution (20 meV). More experiments were latter perform which confirmed that a gap is absent in the $x = 0.1$ samples.

The discrepancy in the gap size and momentum dependence can be explained by three possible scenarios: (I) Disorder in the $x = 0.1$ leads to the broadening of spectral features. However, both NMR [21] and high resolution x-ray diffraction[19] show that the $x = 0.1$ family is the most structurally ordered. (II) A scenario where Δ only opens below T_c, which is different for both samples. Nevertheless, the observation of a Fermi arc for the $x = 0.4$ sample is inconsistent with this scenario. (III) A scenario where both samples are above Tc, but there is an intrinsic difference in their gap size. Recent NMR measurements indicate that in CLBLCO there is a gap above Tc in extreme overdoped samples [35]. This suggests that there is an intrinsic difference in the anti-nodal gap size between the two families

Finally, we compared the nodal Fermi velocity between families. The dispersion in the nodal direction, was measured for each sample in two branches with high statistics. The study was perform on numerous samples from both families to average out misalignment errors, although a strict protocol was employed (described in the supplemental material) to ensure proper alignment. Exemplary dispersion of two samples are shown in Fig. 4. An axis breaker is used in order to show the two branches. Two linear regimes were observed in the data, between $-50 < E < 0$ meV which is closer to E_f and a second regime which extends to high energies of $-150 < E < -50$ meV. Between the two regime a ”kink” was observed which involves the electrons dispersion re-normalized due to correlations [36] or coupling between electrons and low energy bosonic degrees of freedom [37].

The results summarizing the slope of the dispersion $\partial E/\partial k$ which provides the high-energy (v_{HE}) velocity, reside in the inset of Fig. 4. For the $x = 0.1$ family, the average high-energy velocity is $\langle V_{HE}^{0.1} \rangle = 1.53(04)$ eV$\mathring{A}$, while for the $x = 0.4$ it is $\langle V_{HE}^{0.4} \rangle = 1.73(04)$ eV$\mathring{A}$. Despite the velocity distribution overlap, the average velocities differ by

3.5σ, and hence are statistically different with 99.5% confidence. The ratio of velocities $\left(\langle V_{HE}^{0.4}\rangle / \langle V_{HE}^{0.1}\rangle\right)^2 \simeq 1.26 \pm 0.08$. Despite the large error-bar, this ratio is very close to that expected from the ratio of the super-exchange J between families. This ratio is given by $J(0.4)/J(0.1) = T_c^{max}(0.4)/T_c^{max}(0.1) \simeq 1.4$ (see Fig. 1.4). Therefore, the $J \propto t^2$ relation is obeyed, and T_c^{max} depends on orbital overlaps even when the measurements are done in the doped phase.

The ARPES measurements reveals additional details regarding disorder in CLBLCO. The line width of the energy dispersion curve (EDC) peak at the Fermi momentum (k_f) is a measure of the single particle life time. The line width of the momentum dispersion curve (MDC) at the Fermi energy (E_f) is a measure of the single particle coherence length. No quantitative differences were found between the EDC line widths. The MDC of the x=0.1 sample is broader in the nodal direction, and narrower in the anti-nodal direction. Since the anti-nodal direction is more relevant to HTSC, it seems that from the ARPES point of view, the x=0.1 sample is the cleaner one.

In conclusion, we present ARPES data from CLBLCO. We find that the surface doping is independent of the bulk doping or the Ca to Ba ratio. We also demonstrate that the gap can be measured in this system. The hopping parameter t is larger for $x = 0.4$ than for $x = 0.1$ in the overdoped sides. This suggests that T_c^{max} is correlated with electron-orbital overlaps on neighboring sites.

Comprehensive study of the spin-charge interplay in antiferromagnetic LSCO

Recent low temperature angle-resolved photoemission spectroscopy (ARPES) experiments on the underdoped cuprate superconductors indicate the presence of a fully gapped Fermi surface [13, 14, 38, 39]; even in the antiferromagnetic phase [12]. In this worked we explored the possibility that the nodal gap is a result of spin density waves (SDW). A Large, custom made, single crystal of LSCO allowed for magnetic measurements such as muon spin rotation (μSR) and neutron diffraction (ND), simultaneously with ARPES.

The magnetic probes characterized the SDW while ARPES was used to explores the gap.

For this project a series of LSCO single crystals with ∼0.2-0.3% doping steps around 2% were grown, in search of one crystal on which all the experimental techniques mention above apply. The series of samples are first characterized by μSR. Figure 1 of the article show the μSR frequency as a function of temperature for LSCO single crystals with different x values. For samples with doping crossing 2% a sharp transition occurs from an antiferromagnetic long range order to a spin glass state [40]. The sample with x=1.92% was chosen for the rest of the experiment.

The magnetic structure of the sample has been investigated using neutron diffraction. In Fig.2(b) neutron diffraction measurement at the lowest temperature are depicted. The scan was perform near the $(\pi, -\pi)$ point. A double peak structure with a diagonal orientation has been detected, indicating a broken fourfold symmetry, consistent with an incommensurate SDW previously measured in LSCO [41, 42]. Such incommensurate peaks occur when, on top of the main magnetic order, the system develops spin modulations (stripes) oriented diagonally to the bond directions. The commensurate (π, π) peak was also detected and its temperature dependence has been followed.

Employing ARPES, the electronic spectra of the sample has been examined. The underlying FS of the sample is given in Fig.2(a) and is similar to previously obtained results for LSCO[13]. Most of the intensity is centered around the node, suggesting the presence of gapped electronic excitations in the anti-node. This can be seen more clearly in EDC's along the FS in Fig.4.

The key finding of the current work is described in Fig.3, a nodal gap in the AFM phase of LSCO. At high temperatures ($T > 50$ K), the dispersive peak crosses E_{F} as clearly seen in the figure. In contrast, at low temperatures ($T < 45$ K) there is a gap in the electronic spectra. The nodal gap occur not only in underdoped cuprates but also in in simulations where inhomogeneous SDW and superconductivity coexist [43] or Coulomb disorder effects are present [44]. The position of Fermi momentum k_f during the opening of the gap was also explored. By extracting the MDC's at E_f, we concluded that k_f do not shift as the gap opens.

In Fig.5, we summarizes all the parameters extracted from all three techniques. In the figure, the μSR and magnetic volume fraction, the integrated commensurate and incommensurate signal measured with ND and the size of the nodal gap is plotted against Temperature. The major observations in this figure are: (I) The nodal gap opens at $T = 45$ K. (II) Commensurate magnetism is well developed when the gap opens. (III) Spin density wave forms at the same temperature (more or less) then the gap opening. The temperature mismatch between the opening of the nodal gap appearance of the incommensurate peaks are attributed to time scale difference between the experimental probes.

Although there is an evident link between nodal gap and SDW, they are connected in a non trivial way. For example, the observed incommensurate SDW do not fulfill the nesting condition, $\mathbf{k}_f + \delta = \frac{\sqrt{2}\pi}{2a}$. Moreover, Berg *et al.*[45] claim the commensurate part of the SDW can destabilize the node if the magnetic moments size exceeds a critical value, which can be true in our case. However, such gap must be accompanied with a shift in the position in the Fermi momentum. For the incommensurate part of the SDW, can produce a nodal depending on the properties of time reversal followed by translation symmetry. If the symmetry is conserved, a nodal gap will open only when perturbation which exceeds a critical value. Both options are contradiction to the data presented in our work. If the symmetry is broken, a nodal gap can open for arbitrarily small perturbation with no impact on $\mathbf{k}_f$. From our data, it appears that the incommensurate SDW indeed breaks the symmetry of time reversal followed by translation. Another possibility is that this phenomenon is caused by a fully gapped topological superconducting state that coexists with the anti-ferromagnetic order [46] or by a disorder-induced Coulomb gap [47].

In conclusion, we measured a nodal gap in the AFM phase of $\mathrm{La}_{2-x}\mathrm{Sr}_x$ CuO_4 with $x = 1.92\%$. The gap opens well below T_N and very close to the temperature where incommensurate SDW is detected. This finding puts strong restrictions on the origin of the nodal gap.

Bibliography

[1] J. Bardeen, L. N. Cooper, and J. R. Schrieffer. Theory of superconductivity. *Phys. Rev.*, 108:1175–1204, Dec 1957. doi: 10.1103/PhysRev.108.1175. URL `http://link.aps.org/doi/10.1103/PhysRev.108.1175`.

[2] J. G. Bednorz and K. A. Müller. Possible high T_c superconductivity in the Ba-Ba-Cu-O. *Z. Phys. B:Cond Mat*, 64, 1986.

[3] R. J. Cava et al. Bulk superconductivity at 91 k in single-phase oxygen-deficient perovskite $\mathrm{B}a_2\mathrm{YC}u_3\mathrm{O}_{9-\delta}$. *Phys. Rev. Lett.*, 58(16), 1987.

[4] L. Gao et al. Superconductivity up to 164 k in $\mathrm{H}g\mathrm{B}a_2\mathrm{C}a_{m-1}\mathrm{C}u_m\mathrm{O}_{2m+2+\delta}$ (m=1, 2, and 3) under quasihydrostatic pressures. *Phys. Rev. B*, 50(6):4260–4263, 1994.

[5] J. Orenstein and A. J. Millis. Advances in the physics of high-temperature superconductivity. *Science*, 288(5465), 2000.

[6] E. Torikai K. Nagamine H. Kitazawa, K. Katsumata. Coexistence of magnetic ordering and superconductivity in La-Sr-Cu-O system revealed by positive muon spin relaxation. *Solid State Communications*, 67(12), 1988.

[7] Yoichi Ando, Seiki Komiya, Kouji Segawa, S. Ono, and Y. Kurita. Electronic phase diagram of high-T_c cuprate superconductors from a mapping of the in-plane resistivity curvature. *Phys. Rev. Lett.*, 93:267001, Dec 2004. doi: 10.1103/PhysRevLett.93.267001. URL `http://link.aps.org/doi/10.1103/PhysRevLett.93.267001`.

[8] Tom Timusk and Bryan Statt. The pseudogap in high-temperature superconductors: an experimental survey. *Reports on Progress in Physics*, 62(1):61, 1999. URL `http://stacks.iop.org/0034-4885/62/i=1/a=002`.

[9] A. Kanigel et al. Evolution of the pseudogap from fermi arcs to the nodal liquid. *Nature Physics*, 2:447 – 451, 2006. doi: doi:10.1038/nphys334.

[10] J. Chang, E. Blackburn, a. T. Holmes, N. B. Christensen, J. Larsen, J. Mesot, Ruixing Liang, D. a. Bonn, W. N. Hardy, a. Watenphul, M. V. Zimmermann, E. M. Forgan, and S. M. Hayden. Direct observation of competition between superconductivity and charge density wave orderin YBa2Cu3O6.67. *Nature Physics*, 8(12):871–876, October 2012. ISSN 1745-2473. doi: 10.1038/nphys2456. URL `http://www.nature.com/doifinder/10.1038/nphys2456`.

[11] M. Le Tacon, A. Bosak, S. M. Souliou, G. Dellea, T. Loew, R. Heid, K-P. Bohnen, G. Ghiringhelli, M. Krisch, and B. Keimer. Inelastic x-ray scattering in yba2cu3o6.6 reveals giant phonon anomalies and elastic central peak due to charge-density-wave formation. *Nat Phys*, 10(1):52–58, 01 2014. URL `http://dx.doi.org/10.1038/nphys2805`.

[12] Yingying Peng, Jianqiao Meng, Daixiang Mou, Junfeng He, Lin Zhao, Yue Wu, Guodong Liu, Xiaoli Dong, Shaolong He, Jun Zhang, Xiaoyang Wang, Qinjun Peng, Zhimin Wang, Shenjin Zhang, Feng Yang, Chuangtian Chen, Zuyan Xu, T. K. Lee, and X. J. Zhou. Disappearance of nodal gap across the insulator–superconductor transition in a copper-oxide superconductor. *Nat Commun*, 4, 09 2013. URL `http://dx.doi.org/10.1038/ncomms3459`.

[13] E. Razzoli, G. Drachuck, A. Keren, M. Radovic, N. C. Plumb, J. Chang, Y.-B. Huang, H. Ding, J. Mesot, and M. Shi. Evolution from a nodeless gap to $d_{x^2-y^2}$-wave in underdoped $\mathrm{la}_{2-x}\mathrm{sr}_x\mathrm{cuo}_4$. *Phys. Rev. Lett.*, 110:047004, Jan 2013. doi: 10.1103/PhysRevLett.110.047004. URL `http://link.aps.org/doi/10.1103/PhysRevLett.110.047004`.

[14] I. M. Vishik, M. Hashimoto, Rui-Hua He, Wei-Sheng Lee, Felix Schmitt, Donghui Lu, R. G. Moore, C. Zhang, W. Meevasana, T. Sasagawa, S. Uchida, Kazuhiro Fujita, S. Ishida, M. Ishikado, Yoshiyuki Yoshida, Hiroshi Eisaki, Zahid Hussain, Thomas P. Devereaux, and Zhi-Xun Shen. Phase competition in trisected superconducting dome. *Proceedings of the National Academy of Sciences*, 109(45):

18332–18337, 2012. doi: 10.1073/pnas.1209471109. URL http://www.pnas.org/content/109/45/18332.abstract.

[15] D. Goldschmidt, G. M. Reisner, Y. Direktovitch, A. Knizhnik, E. Gartstein, G. Kimmel, and Y. Eckstein. Tetragonal superconducting family $(\mathrm{ca}_x\mathrm{la}_{1-x})(\mathrm{ba}_{1.75-x}\mathrm{la}_{0.25+x})\mathrm{cu}_3\mathrm{o}_y$: The effect of cosubstitution on the transition temperature. *Phys. Rev. B*, 48:532–542, Jul 1993. doi: 10.1103/PhysRevB.48.532. URL http://link.aps.org/doi/10.1103/PhysRevB.48.532.

[16] O. Chmaissem, Y. Eckstein, and C. G. Kuper. *Phys. Rev. B*, 63, 2001.

[17] A Knizhnik, Y Direktovich, G.M Reisner, D Goldschmidt, C.G Kuper, and Y Eckstein. Transport measurements in the 1-2-3 system {CLBLCO} in both the oxygen-underdoped and -overdoped regions. *Physica C: Superconductivity*, 321:199 – 206, 1999. ISSN 0921-4534. doi: http://dx.doi.org/10.1016/S0921-4534(99)00363-9. URL http://www.sciencedirect.com/science/article/pii/S0921453499003639.

[18] Eran Amit and Amit Keren. Critical-doping universality for cuprate superconductors oxygen nuclear-magnetic-resonance investigation of clblco. *Phys. Rev. B*, 82:172509, 2010.

[19] S. Agrestini, S. Sanna, K. Zheng, R. De Renzi, E. Pusceddu, G. Concas, N.L. Saini, and A. Bianconi. Soft x-ray absorption and high-resolution powder x-ray diffraction study of superconducting caxla1?xba1.75?xla0.25+xcu3oy system. *Journal of Physics and Chemistry of Solids*, 75(2):259 – 264, 2014. ISSN 0022-3697. doi: http://dx.doi.org/10.1016/j.jpcs.2013.09.026. URL http://www.sciencedirect.com/science/article/pii/S0022369713003375.

[20] Dirk Wulferding, Meni Shay, Gil Drachuck, Rinat Ofer, Galina Bazalitsky, Zaher Salman, Peter Lemmens, and Amit Keren. Relation between cuprate superconductivity and magnetism: A raman study of $(\mathrm{CaLa})_1(\mathrm{BaLa})_2\mathrm{cu}_3\mathrm{o}_y$. *Phys. Rev. B*, 90:104511, Sep 2014. doi: 10.1103/PhysRevB.90.104511. URL http://link.aps.org/doi/10.1103/PhysRevB.90.104511.

[21] Amit Keren. Evidence of magnetic mechanism for cuprate superconductivity. *New Journal of Physics*, 11(6):065006, 2009.

[22] Sbastien Marchand, Arlette Trokiner, Andrey Yakubovsky, Arkady Knizhnik, and Yakov Eckstein. Doping dependence of the 43ca knight shift in the normal state of superconducting (la1?xcax)(ba1.75?xla0.25+x)cu3oy. *Physica C: Superconductivity*, 408?410(0):826 – 827, 2004. ISSN 0921-4534. doi: http://dx.doi.org/10.1016/j.physc.2004.03.148. URL `http://www.sciencedirect.com/science/article/pii/S0921453404005544`. Proceedings of the International Conference on Materials and Mechanisms of Superconductivity. High Temperature Superconductors {VII} – {M2SRIO}.

[23] Rinat Ofer, Amit Keren, Omar Chmaissem, and Alex Amato. Universal doping dependence of the ground-state staggered magnetization of cuprate superconductors. *Phys. Rev. B*, 78:140508, 2008.

[24] Rinat Ofer, Galina Bazalitsky, Amit Kanigel, Amit Keren, Assa Auerbach, James S. Lord, and Alex Amato. Magnetic analog of the isotope effect in cuprates. *Phys. Rev. B*, 74:220508, 2006.

[25] Z. Hussain A. Damascelli and Z. Shen. *Rev. Mod. Phys.*, 75(2), 2003.

[26] J.D Axe N. Nakamura S. Uchida J.M Ttanquada, B.J Sterlieb. Evidence for stripe correlations of spins and holes in copper oxide superconductors. *Nature*, 375:561–563, 1995.

[27] S.M. Koohpayeh, D. Fort, and J.S. Abell. The optical floating zone technique: A review of experimental procedures with special reference to oxides. *Progress in Crystal Growth and Characterization of Materials*, 54(3?4):121 – 137, 2008. ISSN 0960-8974. doi: http://dx.doi.org/10.1016/j.pcrysgrow.2008.06.001. URL `http://www.sciencedirect.com/science/article/pii/S096089740800003X`.

[28] G. L. Squires. *Introduction to the Theory of Thermal Neutron Scattering*. 1997. ISBN 0-486-69447-x.

[29] Steve J. Hill. *Inductively Coupled Plasma Spectrometry and its Applications*. Blackwell, 2nd edition edition, 2007.

[30] T. Maitland and S. Sitzman. *Scanning Microscopy for Nanotechnology*. 1st edition edition, 2007.

[31] Henk Eskes and Robert Eder. Hubbard model versus t-j model: The one-particle spectrum. *Phys. Rev. B*, 54:R14226–R14229, Nov 1996. doi: 10.1103/PhysRevB.54.R14226. URL `http://link.aps.org/doi/10.1103/PhysRevB.54.R14226`.

[32] M. A. Hossain, J. D. F. Mottershead, D. Fournier, A. Bostwick, J. L. McChesney, E. Rotenberg, R. Liang, W. N. Hardy, G. A. Sawatzky, I. S. Elfimov, D. A. Bonn, and A. Damascelli. In situ doping control of the surface of high-temperature superconductors. *Nat Phys*, 4(7):527–531, 07 2008. URL `http://dx.doi.org/10.1038/nphys998`.

[33] D. Fournier, G. Levy, Y. Pennec, J. L. McChesney, A. Bostwick, E. Rotenberg, R. Liang, W. N. Hardy, D. A. Bonn, I. S. Elfimov, and A. Damascelli. Loss of nodal quasiparticle integrity in underdoped yba2cu3o6+x. *Nat Phys*, 6(11):905–911, 11 2010. URL `http://dx.doi.org/10.1038/nphys1763`.

[34] R. S. Markiewicz, S. Sahrakorpi, M. Lindroos, Hsin Lin, and A. Bansil. One-band tight-binding model parametrization of the high-T_c cuprates including the effect of k_z dispersion. *Phys. Rev. B*, 72:054519, Aug 2005. doi: 10.1103/PhysRevB.72.054519. URL `http://link.aps.org/doi/10.1103/PhysRevB.72.054519`.

[35] T. Cvitanić, D. Pelc, M. Požek, E. Amit, and A. Keren. $^{17}\mathrm{O} - \mathrm{NMR}$. *Phys. Rev. B*, 90:054508, Aug 2014. doi: 10.1103/PhysRevB.90.054508. URL `http://link.aps.org/doi/10.1103/PhysRevB.90.054508`.

[36] T. Sato, H. Matsui, T. Takahashi, H. Ding, H.-B. Yang, S.-C. Wang, T. Fujii, T. Watanabe, A. Matsuda, T. Terashima, and K. Kadowaki. Observation of band renormalization effects in hole-doped high-T_c superconductors. *Phys. Rev. Lett.*, 91:157003, Oct 2003. doi: 10.1103/PhysRevLett.91.157003. URL `http://link.aps.org/doi/10.1103/PhysRevLett.91.157003`.

[37] A. Lanzara, P. V. Bogdanov, X. J. Zhou, S. A. Kellar, D. L. Feng, E. D. Lu, T. Yoshida, H. Eisaki, A. Fujimori, K. Kishio, J. I. Shimoyama, T. Noda, S. Uchida,

Z. Hussain, and Z. X. Shen. Evidence for ubiquitous strong electron-phonon coupling in high-temperature superconductors. *Nature*, 412(6846):510–514, 08 2001. URL `http://dx.doi.org/10.1038/35087518`.

[38] Tonica Valla. Angle-resolved photoemission from cuprates with static stripes. *Physica C: Superconductivity*, 481(0):66 – 74, 2012. ISSN 0921-4534. doi: http://dx.doi.org/10.1016/j.physc.2012.04.005. URL `http://www.sciencedirect.com/science/article/pii/S0921453412001839`. Stripes and Electronic Liquid Crystals in Strongly Correlated Materials.

[39] John W. Harter, Luigi Maritato, Daniel E. Shai, Eric J. Monkman, Yuefeng Nie, Darrell G. Schlom, and Kyle M. Shen. Nodeless superconducting phase arising from a strong (π, π) antiferromagnetic phase in the infinite-layer electron-doped $\mathrm{la}_{1-x}\mathrm{sr}_x\mathrm{cuo}_4$ compound. *Phys. Rev. Lett.*, 109:267001, Dec 2012. doi: 10.1103/PhysRevLett.109.267001. URL `http://link.aps.org/doi/10.1103/PhysRevLett.109.267001`.

[40] Ch. Niedermayer, C. Bernhard, T. Blasius, A. Golnik, A. Moodenbaugh, and J. I. Budnick. Common phase diagram for antiferromagnetism in $\mathrm{la}_{2-x}\mathrm{sr}_x\mathrm{cuo}_4$ and $Y_{1-x}\mathrm{ca}_x\mathrm{ba}_2\mathrm{cu}_3O_6$ as seen by muon spin rotation. *Phys. Rev. Lett.*, 80:3843–3846, Apr 1998. doi: 10.1103/PhysRevLett.80.3843. URL `http://link.aps.org/doi/10.1103/PhysRevLett.80.3843`.

[41] M. Fujita, K. Yamada, H. Hiraka, P. M. Gehring, S. H. Lee, S. Wakimoto, and G. Shirane. Static magnetic correlations near the insulating-superconducting phase boundary in $\mathrm{la}_{2-x}\mathrm{sr}_x\mathrm{cuo}_4$. *Phys. Rev. B*, 65:064505, Jan 2002. doi: 10.1103/PhysRevB.65.064505. URL `http://link.aps.org/doi/10.1103/PhysRevB.65.064505`.

[42] M. Matsuda, M. Fujita, K. Yamada, R. J. Birgeneau, Y. Endoh, and G. Shirane. Electronic phase separation in lightly doped $\mathrm{la}_{2-x}\mathrm{sr}_x\mathrm{Cuo}_4$. *Phys. Rev. B*, 65:134515, Mar 2002. doi: 10.1103/PhysRevB.65.134515. URL `http://link.aps.org/doi/10.1103/PhysRevB.65.134515`.

[43] W. A. Atkinson, J. David Bazak, and B. M. Andersen. Robust nodal *d*-wave spectrum in simulations of a strongly fluctuating competing order in underdoped cuprate superconductors. *Phys. Rev. Lett.*, 109:267004, Dec 2012. doi: 10.1103/PhysRevLett.109.267004. URL `http://link.aps.org/doi/10.1103/PhysRevLett.109.267004`.

[44] Wei Chen, Giniyat Khaliullin, and Oleg P. Sushkov. Coulomb disorder effects on angle-resolved photoemission and nuclear quadrupole resonance spectra in cuprates. *Phys. Rev. B*, 80:094519, Sep 2009. doi: 10.1103/PhysRevB.80.094519. URL `http://link.aps.org/doi/10.1103/PhysRevB.80.094519`.

[45] E. Berg, C-C. Chen, and S. A. Kivelson. Stability of nodal quasiparticles in superconductors with coexisting orders. *Phys. Rev. Lett.*, 100:027003, Jan 2008. doi: 10.1103/PhysRevLett.100.027003. URL `http://link.aps.org/doi/10.1103/PhysRevLett.100.027003`.

[46] Yuan-Ming Lu, Tao Xiang, and Dung-Hai Lee. Underdoped superconducting cuprates as topological superconductors. *Nature Physics*, 10:634–63, 2014.

[47] Wei Chen, Giniyat Khaliullin, and Oleg P. Sushkov. Coulomb disorder effects on angle-resolved photoemission and nuclear quadrupole resonance spectra in cuprates. *Phys. Rev. B*, 80:094519, Sep 2009. doi: 10.1103/PhysRevB.80.094519. URL `http://link.aps.org/doi/10.1103/PhysRevB.80.094519`.

חקירת המכניזם של מוליכות על בטמפרטורות גבוהות באמצעות גבישים יחידים של CLBLCO

גיל דרצ׳וק

חקירת המכניזם של מוליכות על בטמפרטורות גבוהות באמצעות גבישים יחידים של CLBLCO

חיבור על מחקר

לשם מילוי חלקי של הדרישות לקבלת
התואר דוקטור לפילוסופיה

גיל דרצ׳וק

הוגש לסנט הטכניון – מכון טכנולוגי לישראל
תשרי תשע״ד חיפה אוקטובר 2014

החיבור על מחקר הנעשה בהנחיית פרופ׳ עמית קרן

בפקולטה לפיסיקה

הכרת תודה

אני מודה לפרופ׳ עמית קרן על הנחיה, התמיכה, הסבלנות והעידוד במשך תקופת עבודתי בקבצותו.

אני מודה לפרופ״ח עמית קניגל העזרה הרבה במהלך כל הדוקטורט.

תודה מיוחדת לגלינה בזליצקי על עזרת בהכנת הדגמים וחברתה הנעימה. תודה לטכנאים ד״ר לאוניד יומין ושמואל הוידה על עזרתם.

תודה לכל חברי קבוצת הטמפטורות הנמוכות, לדורותיהם, על התקופה המהנה.

תודה מיוחדת ללינה על האהבה והסבלנות.

נכתב לזכרו של טל קירנז׳נר

אני מודה לטכניון על התמיכה הכספית הנדיבה במשך

השתלמותי.

תקציר

מוליכות העל בטמפרטורות גבוהות התגלתה במוליכי העל הנחושתיים בשנות השמונים של המאה העשרים. מאז גילוי חומרים אלו הושקעו מאמצים רבים ,הן ניסוניים והן תיאורטיים, להבין את המנגנון שאחראי לתופעה זו .לעשרות החומרים השונים שמשתייכים לקטגורית מוליכי העל הנחושתיים תכונות משותפות רבות, מה שמרמז על כך שבכולן מתרחש אותו תהליך פיסיקלי. לכולם יש מבני גבישי פרובסקיטי המכיל מספר מישורי נחושת חמצן המופרדים על ידי יוניות מבודדות. השכבות משמשות כמאגרי מטען חשמלי בעלי יכולת לשנות את מספר החורים במישורי הנחושת חמצן כאשר מחליפים את היונים או מוסיפים חמצן לחומר.

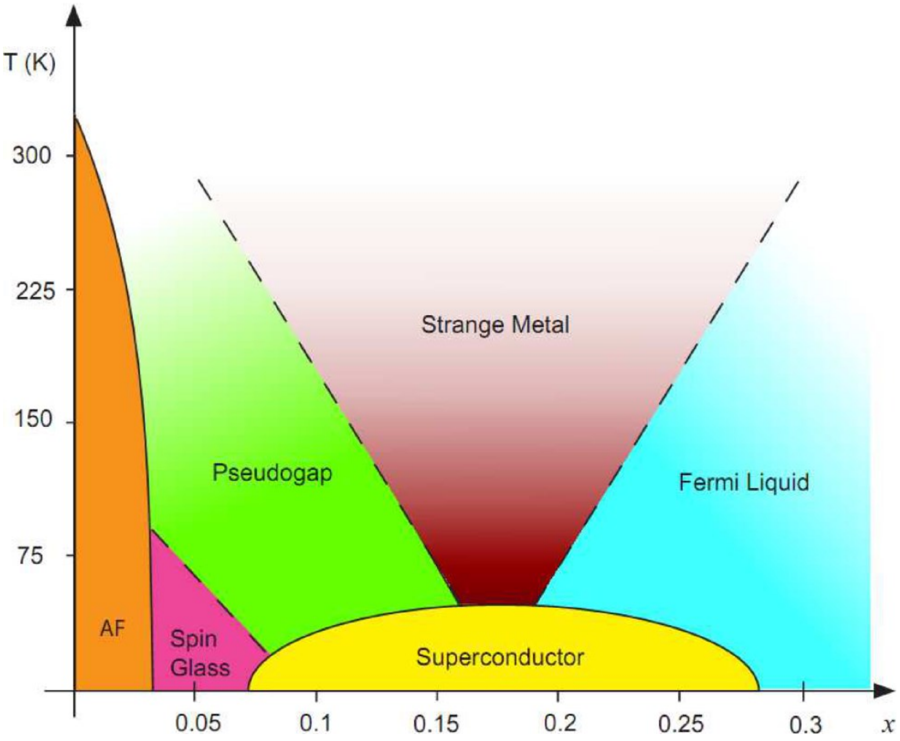

איור 1 דיאגרמת הפאזות של מולכי על נחושתיים

תכונותיהם הפיסיקליות של מוליכי העל הנחושתיים ניתנים לשינוי באמצעות שינוי מספר החורים (סימום). מצב היסוד של חומרים אלו הוא אנטיפרומגנטי: הספינים האלקטרונים של אטומי הנחושת הסמוכים מסודרים בכיוונים הפוכים. במצב זה החומר הינו מבודד מסוג מוט. כאשר מוסיפים חורים למישורים, העל מוליכים טמפרטורת המעבר לפאזה יורדת ובהמשך נעלמת, ומצב היסוד של החומר הופך לזכוכיתי, סדר אנטיפרומגנטי קצר טווח. גם טמפרטורת המעבר לפאזה הזכוכיתית יורדת כאשר מוסיפים חורים , ולבסוף נעלמת. לאחר סימום מספק של החומר מצב היסוד הוא מוליכות על. התלות של טמפרטורת המעבר לפאזה זו במספר החורים נראית כקשת

בעלת ערך מכסימלי המאפיין את החומר (טמפרטורת מעבר מכסימלית לפאזה העל מוליכה). בפאזה העל מוליכה השדות החשמלים והמגנטים החומר הם אפס.

בניגוד למוליכי על מתכתיים בהם הפיסיקה מוסברת ע״י תורת BCS ופרמטר הסדר ופונקציית פער האנרגיה הם מסימטריית S-wave, לעל מוליכים הנחושתיים פרמטר הסדר ופונקציית פער האנרגיה הינם מסימטרייה D-wave. כמו כן אין תאוריה סגורה המתארת את הפיסיקה של חומרים אלו. כאשרי הסימום של מוליכי העל הוא גבוה מהערך האופטימלי, הערך בו טמפרטורת המעבר למצב העל מוליך היא הגבוה ביותר, פער האנרגיה של מוליך העל נסגרת מעל הטמפרטורה הקריטית. כאשרי הסימום של מוליכי העל נמוך מהערך האופטימלי, ישנו פער אנרגיה הנקרא פסאודוגאפ והוא נמשך לטמפרטורות גבוהות בהרבה מהטמפרטורה הקריטית. מצד אחד, הפסאודוגאפ יכול להוות עדות לכך שיש זוגות קופר על מוליכים הנוצרים מעל לטמפרטורת המעבר, אך במצב זה אין קורלציות ארוכות טווח של פרמטר הסדר העל מוליך. מצד שני, יש הטוענים שפסאודוגאפ הינו עדות לפרמטרי סדר המתחרים בעל מוליכות ואינם קשורים אליה ישירות.

בעבודה זו נחקרו שני חומרים מקבוצת מוליכי העל הנחושתיים בצורה של גבישים יחידים. החומר $(Ca_xLa_{1-x})(Ba_{1.75-x}La_{0.25+x})Cu_3O_y$ הינו מוליך על נחושתי, הסונתז לראשונה בטכניון. החומר מספק ״מגרש משחקים ניסיוני״ היחודי לחומר ועשוי לשפוך אור על המנגנון של מוליכות על בטמפרטורות גבוהות. המבנה הגבישי CLBLCO הוא דומה ל-YBCO. אף על פי כן, שלא כמו YBCO, CLBLCO הוא טטרגונלי עבור כל הערכים של x וy ואין לו שרשרת חמצן מסודרות מחוץ למישורים. בנוסף יש ב-CLBLCO שני פרמטרים שניתן לשנות בהרכב הכימי; x יחס הסידן לבריום וy כמות החמצן הכולל. ב-CLBLCO יש שני מישרוי נחושת חמצן, במרכז התא היחידה, מופרדים על ידי קטיון סידן או לנתנום. התכונות הפיסיקליות של CLBLCO תלויים בשני המשתנים ושינויים שיטתיים ברורים נתגלו על ידי שינוי x. ניתן להגדיר ארבע משפחות של CLBLCO, עם ערכי x של $x = 0.1, 0.2, 0.3$ ו0.4. אמנם לכל משפחה יש CLBLCO דיאגרמת פאזה שונה הם חולקים מוצא משותף ועל כך מסופר בתזה.

החומר השני הינו $La_{2-x}Sr_xCuO_4$ (LSCO). הסימום של החומר נעשה על ידי הוספה של סטרונציום (Sr) במקום הלאנטאנום (La). בדרך זו ניתן לשנות את ריכוז החורים נושאי המטען במישורי החמצן-נחושת ובכך להעביר את החומר ממצב של מבודד מוט למצב של מוליכות על, ובנוסף לשלוט על הטמפרטורה הקריטית.

עבודה זו מחולקת לשלושה חלקים ותוצאות מסוכמות במאמרים שהתפרסמו בספרות המדעית:

במאמר הראשון אנו מדווחים על הגידול המוצלח של גבישים יחידים של החומר CLBLCO. הגבישים היחידים גודלו באמצעות טכניקת ה״אזור המותך הנע״. בטכניקה זו משתמשים בתנור בתוכו ממוקמות ארבע מראות פרבוליות ובמרכזן מורכבות מנורות בעלות הספק גבוה. המראות

מרכזות את האור אל מוט קרמי מהחומר אותו רוצים לגדל ויוצרות בו אזור נוזלי מותך אשר מועבר בקצב איטי לאורך כל המוט ומתוך הנוזל המותך המוצק מתגבש לגביש יחיד. הגבישים היחדים שגודלו אופיינו במגוון שיטות נסיוניות כגון : מדידות התנגדות, מדידות של השבר החלקי העל מוליך, סיבוב סחריר המיואון, פיזור ניוטרונים ופיזור ראמאן. התוצאות שקיבלנו מצביעות על כך שהגבישים שגדלו ניתנים לביקוע וחושפים משטחים נקיים וחלקים ובכך הופך אותם למתאימים עבור טכניקות הרגישות לאיכות פני השטח. כמו כן גילינו שהגבישים הם בעלי תכונות דומות לאבקות המקוריות מהן גודלו הגבישים. תכונות אלה בשילוב עם דיאגרמת הפאזות הייחודית של CLBLCO פתחה פתח למגוון ניסויים חדשים בתחום העל מוליכות הנחושתית.

במאמר השני אנו מראים תוצאות של מדידות ספקטרוסקופית אלקטרונים תלוית זווית (ARPES) בחומר CLBLCO. בניסוי בחנו שתי משפחות, $x=0.1$ ו $x=0.4$ בעלות טמפרטורה קריטית מקסימלית של 56 ו82 מעלות קלווין בהתאמה. המשטח פרמי של נמצא להיות לא תלוי בx או y הראשוניים של הגבישים. הגודל הנמדד של משטח פרמי מעיד על כך שהפני שטח עוברים בניה מחדש של מטען החשמלי ונמצאים במצב של סימום יתר. האוניברסליות של משטח הפרמי אפשר לנו להשוות את התכונות הדינמיות של מוליכי על בעלי מבנה וסימום זהים. מצאנו שבאנרגיות גבוהות, המהירות של האלקטרונים בכיוון בו מתאפס פרמטר הסדר העל מוליך גבוהה יותר עבור המשפחה עם $x=0.4$. מהממצאים משתמע כי קיים קשר ישיר בין הטמפרטורה הקריטית המקסימלית וקצב הקפיצה של האלקטרונים t . ממצאים אלו תומכים ברעיון שבו העל מוליכות הנחושתית מונעת על ידי אנרגיה קינטית.

במאמר השלישי בדקנו את הקשר בין הפסאודוגאפ לסדר מגנטי במוליך על נחושתי מסוג LSCO. בפרט נבחן פער האנרגיה בכיוון האלכסוני שנתגלה לאחרונה באמצעות מגוון טכניקות נסיונית אשר יושמו על גביש יחיד אחד, אשר תוכנן ויוצר במיוחד עבור ניסוי זה. הגביש הינו בעל סדר אנטיפרומגנטי בעל סימום נמוך של חורים. על הגביש ביצענו מדידות מדידות ספקטרוסקופית אלקטרונים תלוית זווית כתלות בטמפרטורה. במדידות זיהינו מספר מאפיינים שמדגימים שהדגם שהכנו היה באיכות גבוהה. הממצא המשמעותי ביותר היה פער האנרגיה בכיוון האלכסוני שנמדד מתחת לטמפרטורה של 45 מעלות קלווין. מדידת קצב סיבוב סחריר המיואון, אישרה את זה שהדגם שלנו הוא אנטיפרומגנטי וכן שהסימום שלו הוא קרוב אך עדיין מתחת לתחום של מצב הספין הזכוכיתי. כמו כן, באמצעות פיזור ניטרונים אלסטי מדדנו את התלות בטמפרטורה של הסדר המגנטי היחסי והלא יחסי וגילינו כי פאר האנרגיה בכיוון האלכסוני נפתח מתחת לטמפרטורה של הסדר היחסי, 140K, אם זאת קרוב מאוד לטמפרטורה של הגל ספינים המגנטי הלא יחסי שמתפתח בטמפרטורה של 30K.

העבודה מסודרת כדלקמן:

- פרק 1 ניתן הרקע לעבודה שלנו.
- פרק 2 מתאר את המערכות בהן השתמשנו להכנת הדגמים בניסוי, וכמו כן מוצגות הטכניקות הניסיניות בהן התשמשנו.
- בפרק 3 מובאות התוצאות של העבודה כמאמרים שפורסמו בספרות המדעית.
- פרק 4 מציג דיון בתוצאות שפורסמו במאמרים.